

Bubble deformation by a turbulent flow

Stéphane Perrard^{1,2}, Aliénor Rivière^{1,2}, Wouter Mostert^{1,3} and Luc Deike^{1,4,†}

¹Department of Mechanical and Aerospace Engineering, Princeton University, Princeton, NJ 08544, USA

²LPENS, Département de Physique, Ecole Normale Supérieure, PSL University, 75005 Paris, France

³Department of Mechanical and Aerospace Engineering, Missouri University of Science and Technology, Rolla, MO 65401, USA

⁴High Meadows Environmental Institute, Princeton University, Princeton, NJ 08544, USA

(Received 22 May 2020; revised 2 April 2021; accepted 20 April 2021)

We investigate the modes of deformation of an initially spherical bubble immersed in a homogeneous and isotropic turbulent background flow. We perform direct numerical simulations of the two-phase incompressible Navier–Stokes equations, considering a low-density bubble in the high-density turbulent flow at various Weber numbers (the ratio of turbulent and surface tension forces) using the air–water density ratio. We discuss a theoretical framework for the bubble deformation in a turbulent flow using a spherical harmonic decomposition. We propose, for each mode of bubble deformation, a forcing term given by the statistics of velocity and pressure fluctuations, evaluated on a sphere of the same radius. This approach formally relates the bubble deformation and the background turbulent velocity fluctuations, in the limit of small deformations. The growth of the total surface deformation and of each individual mode is computed from the direct numerical simulations using an appropriate Voronoi decomposition of the bubble surface. We show that two successive temporal regimes occur: the first regime corresponds to deformations driven only by inertial forces, with the interface deformation growing linearly in time, in agreement with the model predictions, whereas the second regime results from a balance between inertial forces and surface tension. The transition time between the two regimes is given by the period of the first Rayleigh mode of bubble oscillation. We discuss how our approach can be used to relate the bubble lifetime to the turbulence statistics and eventually show that at high Weber numbers, bubble lifetime can be deduced from the statistics of turbulent fluctuations at the bubble scale.

Key words: bubble dynamics, multiphase flow

† Email address for correspondence: ldeike@princeton.edu

1. Introduction

The interaction of turbulent flow with a free surface occurs in numerous physical systems such as ocean waves forced by the turbulent wind (Phillips 1957; Perrard *et al.* 2019), river surface patterns driven by underwater turbulence (Peregrine 1976; Brocchini & Peregrine 2001) and drops and bubbles in turbulent flow (Balachandar & Eaton 2010; Elghobashi 2019; Mathai, Lohse & Sun 2020).

Deformation and break-up of bubbles and droplets in a turbulent flow control exchanges of heat, mass and momentum in numerous natural and engineering processes, for example, in bubble-mediated gas exchange at the ocean–atmosphere surface (Deike & Melville 2018; Reichl & Deike 2020), chemical reactors (Risso 2018), the fall of rain drops (Villermaux & Bossa 2009), the evaporation of sea spray in a turbulent boundary layer (Veron 2015), dynamics of water droplets in clouds (Balachandar & Eaton 2010) and industrial liquid atomization and fragmentation (Eggers & Villermaux 2008).

The dynamics of a single bubble evolving freely in low-viscosity liquid at rest has been extensively studied, with analytical and experimental results describing bubble oscillations (Miller & Scriven 1968; Prosperetti 1980), rise velocity (Moore 1965; Maxworthy *et al.* 1996) and path instability (Magnaudet & Eames 2000; Ern *et al.* 2012). The rise dynamics is altered once bubbles are close enough to each other and can interact through their wakes (Harper 1970; Yuan & Prosperetti 1994), a process that leads to collective effects and bubble-induced turbulence dynamics (Lance & Bataille 1991; Risso 2018).

The deformation dynamics and potential break-up of a bubble depend primarily on the ability of the surrounding fluid to deform the bubble against surface tension forces. This defines the Weber number, comparing inertial forces generated by the turbulent carrier flow and the capillary cohesive forces. Considering the velocity fluctuation at the bubble diameter scale d_0 , formalized by the longitudinal velocity increment $\delta u(\mathbf{d}_0) = u_L(\mathbf{r}, t) - u_L(\mathbf{r} + \mathbf{d}_0, t)$, where u_L is the velocity component along the direction of \mathbf{d}_0 , the turbulent Weber number is defined as $We = \rho_\ell \langle \delta u(d_0)^2 \rangle d_0 / \gamma$ (Hinze 1955; Risso & Fabre 1998), with ρ_ℓ the density of water, γ the air–water surface tension and $\langle \rangle$ the average over the flow configurations. In a homogeneous and isotropic turbulent flow, the velocity fluctuations at the bubble scale $\delta u(d_0)^2$ can be related to the mean dissipation rate of energy ϵ using Kolmogorov (1941) theory, yielding $\langle \delta u(d_0)^2 \rangle = C(\epsilon d_0)^{2/3}$ for d_0 in the inertial range. Experimental studies have observed $C \in [2, 2.2]$ depending on the Reynolds number (Pope 2000; Cowen & Variano 2008). We chose $C = 2$ for consistency with Risso & Fabre (1998), and the Weber number eventually reads as

$$We = \frac{2\rho_\ell \epsilon^{2/3} d_0^{5/3}}{\gamma} \quad (1.1)$$

for a bubble of diameter d_0 immersed in a homogeneous and isotropic turbulent flow. Experimental studies of bubble dynamics in turbulence have identified a critical Weber number We_c of order unity, above which the occurrence of break-up becomes statistically dominant. The value of We_c reported from laboratory experiments varies among authors in the range [1,5], corresponding to variation in experimental conditions, which introduces other flow parameters such as large-scale shear or spatial variations in the dissipation rate (Martinez-Bazan, Montanes & Lasheras 1999; Andersson & Andersson 2006; Ravelet, Colin & Risso 2011; Vejražka, Zedníková & Stanovský 2018). Note also that the critical Weber number is defined statistically, and can be influenced by the temporal and spatial windows of observation of the bubbles. In this paper we consider $We_c = 3$, in accordance with our numerical dataset, obtained from an ensemble of simulations. Two mechanisms driving the deformation and break-up have been discussed (Martinez-Bazan *et al.* 1999;

Andersson & Andersson 2006; Ravelet *et al.* 2011; Vejražka *et al.* 2018), either the direct strong action of an eddy at the scale of the bubble leading to large deformation and break-up, or a resonance mechanism between deformation caused by weaker eddies and oscillations of the bubble (Risso & Fabre 1998). Experimental studies have identified an oscillatory response of bubbles in turbulence associated to the second eigenmode (Risso & Fabre 1998; Ravelet *et al.* 2011). Such an oscillatory response of millimetric bubbles, associated with surface tension forces, is characteristic of the large deformation observed prior to break-up, and corresponds to a much lower frequency than the acoustic mode of deformation, characterized by the Minnaert frequency (Minnaert 1933; Deane & Stokes 2002).

In such configurations the gas–liquid interface is surrounded by a stochastic turbulent flow, characterized by perturbations of various strengths at various scales. In this paper we discuss a theoretical framework of bubble oscillations to describe the temporal evolution of the bubble interface deformation while immersed in a turbulent background flow. To do so, we consider linearized deformations and we neglect any feedback of the interface on the statistics of the turbulent background flow. Our framework has two main inspirations. On one hand, it extends the spherical harmonic decomposition of bubble deformation (Miller & Scriven 1968; Prosperetti 1980) to the presence of external forcing. On the other hand, it is analogous to a liquid–gas interface interpreted as a collection of harmonic oscillators which are forced by a turbulent background flow (Risso & Fabre 1998; Lallane, Masbernat & Risso 2019). This is similar to the case of wind wave generation by pressure fluctuations in a turbulent boundary layer, as proposed by Perrard *et al.* (2019) and built on earlier work by Phillips (1957). However, as we will see, the solutions describing the growth of the bubble interface deformation lie in a different dynamical regime, in which a large separation of time scales between stochastic growth and saturation is not fulfilled, in part because the turbulent forcing occurs in the dense liquid, imposing a rapid response from the gas phase, contrary to forcing in the turbulent air of much weaker inertia inducing deformation at the surface of the dense liquid phase.

We aim to estimate the turbulent excitation in terms of pressure and velocity statistics evaluated on the bubble surface. The utility of the present theoretical framework hence lies on the ability to test numerically the relationship between surface deformation and turbulent background flow statistics.

We discuss an equation linking the growth of the bubble deformation decomposed in spherical harmonics to the turbulence statistics. Doing so, we identify different regimes. At short time, for $t \ll t_2, t_c$, where t_2 is the capillary time describing the oscillatory response of the bubble and t_c is the eddy turnover time at the scale of the bubble, the bubble response is independent of surface tension (Weber number) and the total bubble deformation ζ_Ω follows a linear scaling $\zeta_\Omega \sim t$. The amplitudes of the spherical harmonics coefficients also follow a linear growth in time, while the response is dominated by the modes 2 of oscillation. At an intermediate time scale $t_2 < t < t_c$, bubble deformations are described by a sublinear regime, where the transition time is a function of surface tension (Weber number). The model is evaluated by direct numerical simulations of bubble deformation and break-up in a turbulent flow, resolving the full two-phase air–water Navier–Stokes equations. We compute the bubble deformation, as well as the evolution of the various dynamical modes of deformation. We observe very good agreement between the simulations and the model and observe the different regimes discussed theoretically. Finally, at long time, the bubble deformation either saturates or the bubble breaks, both regimes not being described by our linear model but captured in the simulations. We eventually link the bubble deformation growth to the statistical properties of the

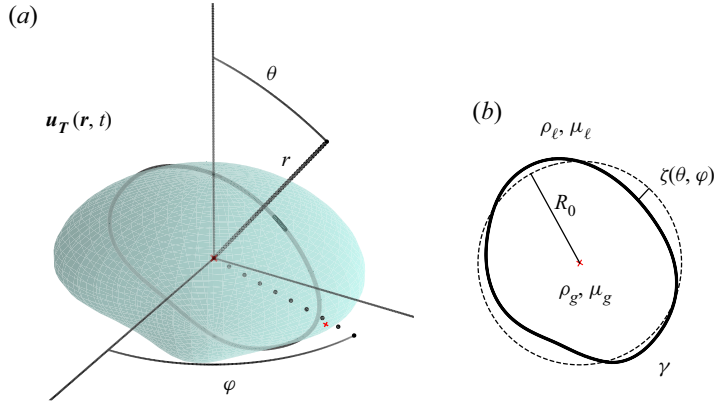


Figure 1. Bubble deformation in a turbulent flow: sketch and definitions.

velocity increments. Doing so, we provide an estimate of the bubble lifetime statistics, which is parametrized by the Reynolds number and Weber number.

The paper is organized as follows. In § 2 we present the theory, while in § 3 we present the simulations and comparison with the theoretical prediction. Conclusions and discussions are presented in § 4.

2. Bubble deformation in a turbulent flow

2.1. Bubble oscillation in a fluid at rest

We consider an incompressible, initially spherical gas bubble of radius $R_0 = d_0/2$, density ρ_g and viscosity μ_g , immersed in a liquid at rest of liquid density ρ_l , viscosity μ_l and surface tension between the gas and the liquid phase γ . The origin of space is set at the centre of mass of the bubble.

The chosen frame of reference is then non-inertial. Note that we do not study here the motion of the centre of mass but aim at a description of the bubble deformation. Focusing on the early stage, we limit our description to a bubble surface that can be parametrized in spherical coordinates (r, θ, φ) by the single-valued distance $R = (R_0(t) + \zeta(\theta, \varphi, t))\hat{r}$ to the centre (figure 1). We aim for a phenomenological set of equations for the modes of deformation of the bubble in the presence of a turbulent background flow, inspired by the forced oscillator model from Risso & Fabre (1998) and Lalanne *et al.* (2019).

To decompose the bubble surface into a basis adapted to the spherical geometry, we introduce the spherical harmonic functions $H_{\ell,m}(\theta, \varphi)$,

$$H_{\ell,m}(\theta, \varphi) = \sqrt{\frac{(2\ell + 1)(\ell - m)!}{(\ell + m)!}} P_{\ell}^m(\cos \theta) e^{im\varphi}, \quad (2.1)$$

with $\ell \in \mathbb{N}$ and $m \in [-\ell, \ell]$, and P_{ℓ}^m is the associated Legendre polynomial. The real form $Y_{\ell,m}(\theta, \varphi)$ of the spherical harmonics reads as

$$Y_{\ell}^m = \begin{cases} \sqrt{2}(-1)^m \text{Im}(H_{\ell}^{-m}) & \text{if } m < 0, \\ H_{\ell}^0 & \text{if } m = 0, \\ \sqrt{2}(-1)^m \text{Re}(H_{\ell}^m) & \text{if } m > 0. \end{cases} \quad (2.2)$$

Bubble deformation by a turbulent background

The real spherical harmonics Y_ℓ^m verifies $\forall \ell \in \mathbb{N}, \forall m \in [-\ell, \ell], \nabla^2 r^{-\ell} Y_\ell^m = 0$ for $r > 0$. In this basis, the expression of the bubble surface $R(\theta, \varphi, t)$ reads as

$$R(\theta, \varphi, t) = R_0(t) + \sum_{\ell=2}^{+\infty} \sum_{m=-\ell}^{\ell} a_{\ell,m}(t) Y_\ell^m(\theta, \varphi), \quad (2.3)$$

where $R_0(t)$ is the mean bubble radius. In the following, we neglect the radius variation associated with gas compressibility and we assume that R_0 is independent of time. In the absence of any background flow, at the linear order in the deformation amplitude ζ/R_0 and small viscous dissipation in the bubble boundary layer, the coefficients $a_{\ell,m}$ are solutions of a set of oscillator equations of the form (Prosperetti 1980)

$$\ddot{a}_{\ell,m} + 2\beta_\ell \dot{a}_{\ell,m} + (\ell - 1)(\ell + 1)(\ell + 2)\omega_0^2 a_{\ell,m} = 0, \quad (2.4)$$

where \cdot denotes the time derivative, $\omega_0 = \sqrt{\gamma/(R_0^3 \rho_\ell)}$ is the typical angular frequency associated with bubble oscillation and β_ℓ is the damping coefficient of mode ℓ . The expression of β_2 is summarized in Lalanne *et al.* (2019) for low viscosity, and the general formula can be found in Miller & Scriven (1968). We introduce $\omega_\ell = \omega_0 \sqrt{(\ell - 1)(\ell + 1)(\ell + 2)}$ the angular frequency associated to mode ℓ and the associated characteristic time $t_\ell = 1/\omega_\ell$ of mode ℓ . We have, in particular, $\omega_2 = 2\sqrt{3}\omega_0$.

2.2. Bubble oscillation in a turbulent background flow

We consider that the bubble is immersed in a liquid animated by turbulent motion, with a velocity $\mathbf{u}(\mathbf{r}, t)$ and a pressure field $p(\mathbf{r}, t)$. In the general case, modelling the action of the turbulent background flow on a bubble is particularly complex. A two-way coupling between the velocity fluctuations near the bubble interface and the interface deformation may take place. The turbulent flow deforms the bubble under the action of normal and tangential stresses, and the turbulent flow statistics can be modified in the immediate vicinity of the bubble interface. In order to construct a phenomenological model for the modes of deformation of the bubble, we follow the approach of Risso & Fabre (1998) and Lalanne *et al.* (2019), which considers a dynamical equation for the second mode of deformation a_2 , assumed to be the main mode excited by the flow. The amplitude $a_2(t)$ then represents the oscillation of the bubble between an oblate and a prolate shape.

We introduce two adaptations of the formulation of Risso & Fabre (1998) and Lalanne *et al.* (2019). (i) We consider that the turbulent flow can excite other modes (ℓ, m) of deformation. The contribution of these higher-order modes ($\ell > 2$) could be non-negligible for high Weber numbers ($We \gg We_c$). (ii) We aim to estimate the turbulent excitation in terms of pressure and velocity statistics evaluated on a sphere of the same radius, in the bulk of the turbulent flow. We perform a linear expansion in the amplitude of the modes of deformation, and we neglect the effect of the interface on the turbulent statistics in its immediate vicinity. The decoupling approach was first motivated by the high-Weber-number case, in which capillary forces are small compared with inertial forces. For a lower Weber number ($We \approx We_c$), our approach is expected to still hold at short time compared with the response time $1/\omega_\ell$. We also consider a large dissipative time compared with the bubble period of oscillation ($\omega_\ell/\beta_\ell \gg 1$), such that we neglect the viscous dissipation. For all these reasons, the following approach is rather phenomenological and by no means exact. The validity of our approach is further discussed by comparison with direct numerical simulations of a single bubble of initial spherical shape deformed by a homogeneous and isotropic turbulent flow.

At the linear order of deformation ($a_{\ell,m}/R_0 \ll 1$), we assume that the bubble surface can still be described by a set of oscillatory equations, adding a forcing term that represents the turbulent background flow

$$\ddot{a}_{\ell,m} + \omega_\ell^2 a_{\ell,m} = F_{\ell,m}, \tag{2.5}$$

where $F_{\ell,m}$ is a function of $\mathbf{u}(\mathbf{R}, t)$, $d\mathbf{u}/dt(\mathbf{R}, t)$ and $p(\mathbf{R}, t)$, respectively, the velocity field, the acceleration field and the pressure field evaluated at the surface of the bubble. We neglect the shear contribution and, looking at the early-time dynamics, we neglect viscous dissipation. To specify the function $F_{\ell,m}$, we introduce the spherical harmonic decomposition of $u_r(R_0\hat{\mathbf{r}}, t) = \mathbf{u} \cdot \hat{\mathbf{r}}$ and $p(R_0\hat{\mathbf{r}}, t)$ evaluated on a sphere of radius R_0 ,

$$u_r(R_0\hat{\mathbf{r}}, t) = \sum_{\ell=2}^{+\infty} \sum_{m=-\ell}^{\ell} u_{\ell,m}(t) Y_\ell^m(\theta, \varphi), \tag{2.6}$$

$$p(R_0\hat{\mathbf{r}}, t) = \rho_\ell \sum_{\ell=2}^{+\infty} \sum_{m=-\ell}^{\ell} \pi_{\ell,m}(t) Y_\ell^m(\theta, \varphi), \tag{2.7}$$

where $\hat{\mathbf{r}}$ is the unit vector along \mathbf{r} . We then approximate the fields $\mathbf{u}(\mathbf{R}, t)$, $d\mathbf{u}/dt(\mathbf{R}, t)$ and $p(\mathbf{R}, t)$ by their value on an undeformed bubble, whose interface position is $R_0\hat{\mathbf{r}}$. Doing so, we neglect the contribution of cross-terms of the type $a_{\ell,m}u_{\ell',m'}$ and terms of $a_{\ell,m}, u_{\ell',m'}, \pi_{\ell',m'}$ of quadratic and higher order. In this limit, the coefficients of the spherical harmonic decomposition of $\dot{u}_r(R_0\hat{\mathbf{r}}, t)$ become $\dot{u}_{\ell,m}$ as $R_0\hat{\mathbf{r}}$ is independent of time. We also neglect the coupling between two different spherical harmonic modes (ℓ, m) and (ℓ', m') which arises at least at the order $a_{\ell,m}u_{\ell',m'}$ or $a_{\ell,m}\pi_{\ell',m'}$. For $a_{\ell,m}/R_0 \ll 1$, we then assume that $F_{\ell,m}$ is a linear function of $u_{\ell,m}, \dot{u}_{\ell,m}$ and $\pi_{\ell,m}$, and we postulate the following form:

$$\ddot{a}_{\ell,m} + \omega_\ell^2 a_{\ell,m} = \dot{u}_{\ell,m} + \frac{C(\ell)}{R_0} \pi_{\ell,m}. \tag{2.8}$$

Here C is a function of ℓ . The kinematic boundary conditions at $t = 0$ give $R(\theta, \varphi, 0) = R_0$ and $\dot{R}(\theta, \varphi, 0) = u_r(R_0, \theta, \varphi, 0)$, which gives the initial conditions for $a_{\ell,m}$,

$$a_{\ell,m}(0) = 0; \quad \text{and} \quad \dot{a}_{\ell,m}(0) = u_{\ell,m}(0). \tag{2.9a,b}$$

2.3. Link with surface deformation

We seek for an estimate of the average global surface deformation. We introduce the root mean squared ζ_Ω of the bubble interface from an integration over all solid angles,

$$\zeta_\Omega^2 = \frac{1}{4\pi} \iint d\Omega \zeta^2. \tag{2.10}$$

According to the orthogonality of spherical harmonics $(1/4\pi) \iint d\Omega Y_\ell^m Y_{\ell'}^{m'} = \delta_{\ell,\ell'} \delta_{m,m'}$, ζ_Ω can be expressed as

$$\zeta_\Omega^2(t) = \sum_{\ell=2}^{+\infty} \sum_{m=-\ell}^{\ell} a_{\ell,m}(t)^2. \tag{2.11}$$

The surface deformation is then related to the solutions of (2.8). The coefficients $a_{\ell,m}$ being stochastic variables, we look for their temporal behaviour as well as temporal behaviour of their ensemble-averaged values $\langle a_{\ell,m}^2 \rangle$.

2.4. Controlling time scales

The solutions of (2.8) depend on the various time scales that are inherently associated to a noise-excited oscillator. For a bubble evolving in a turbulent flow, previous studies have clearly identified one controlling time scale, the natural bubble oscillation response occurring at a capillary time scale (Risso & Fabre 1998; Ravelet *et al.* 2011). Another relevant time scale lies in the turbulence correlation time of the fluctuations at the bubble scale also discussed by several authors (Risso & Fabre 1998; Martinez-Bazan *et al.* 1999; Ravelet *et al.* 2011). Depending on the Weber number, another time scale is eventually given either by the bubble lifetime or the saturation time.

The modes $\ell = 2$ carry most of the surface energy as they correspond to the largest available spatial scale. Therefore, the typical characteristic amplitude and time scales of ζ_Ω are set by the modes $\ell = 2$ of oscillation. The first relevant time scale is the oscillator reduced period $t_2 = 1/\omega_2$ of the second mode $\ell = 2$ of oscillation, which has been proven to dominate the deformation (Risso & Fabre 1998). On a time significantly shorter than the reduced period $\omega_2 t < 1$, the response will be purely inertial and independent of surface tension (Risso & Fabre 1998).

The second characteristic time scale arises from the turbulence temporal correlations $\tau_{\ell,m}$ and $\tilde{\tau}_{\ell,m}$ of, respectively, the coefficients $u_{\ell,m}$ and $\pi_{\ell,m}$ of the spherical decomposition of the velocity and pressure fluctuations. They can be defined from the autocorrelation functions of velocity and pressure, respectively, i.e.

$$\tau_{\ell,m} = \frac{1}{\langle u_{\ell,m}^2 \rangle} \int_{-\infty}^{+\infty} ds \langle u_{\ell,m}(t) u_{\ell,m}(t+s) \rangle. \quad (2.12)$$

$$\tilde{\tau}_{\ell,m} = \frac{1}{\langle \pi_{\ell,m}^2 \rangle} \int_{-\infty}^{+\infty} ds \langle \pi_{\ell,m}(t) \pi_{\ell,m}(t+s) \rangle. \quad (2.13)$$

The estimate of $\tau_{\ell,m}$ presents some difficulties, as there is no clear consensus on the time scales in turbulence. The velocity fluctuations we consider here are neither associated with the Eulerian frame of reference nor a local Lagrangian framework. To provide an estimate of the time scale $\tau_{2,m}$ of the dominant mode of deformation, we consider the time scales t_E and t_L , respectively, of the Eulerian velocity increments and the Lagrangian velocity increments at the bubble scale. The ratio t_E/t_L scales as $(Re_\lambda)^{1/2}$ from the random sweeping hypothesis (Tennekes 1975), such that t_E and t_L can respectively be considered as lower and upper bounds of the correlation time $\tau_{2,m}$. The frozen Taylor hypothesis will henceforth be considered as valid for $t < t_E$, and we estimate $\tilde{\tau}_{2,m}$ from the eddy turnover time at the bubble scale $t_c = \epsilon^{-1/3} d_0^{2/3}$. The correlation times $\tau_{\ell,m}$ and $\tilde{\tau}_{\ell,m}$ of the higher-order modes ($\ell > 2$) are expected to scale as $\ell^{-2/3}$ whereas the capillary time $1/\omega_\ell$ scales as $\ell^{-3/2}$. The criterion $\omega_2 \tau_2 < 1$ therefore implies that $\omega_\ell \tau_\ell < 1$ for higher values of ℓ .

Figure 2 shows the ratio of the typical capillary time scales (t_0 and t_2) with the eddy turnover time scale t_c as a function of Weber number. Below the critical value $We < We_c$ with $We_c = 3$, we have $t_2 \ll t_c$, and this separation persists at moderate We while being reduced. The crossover between these two time scales, $t_2 = t_c$, occurs at higher Weber number, namely $We = 192$ (and $\omega_2 = \sqrt{192}/(t_c \sqrt{We})$). For reference, we provide typical time scales in table 1, corresponding to experimental conditions of bubbles evolving in turbulent flow created from underwater turbulent jets (Risso & Fabre 1998; Martinez-Bazan *et al.* 1999; Vejražka *et al.* 2018; Ruth *et al.* 2019). Note that these experimental systems can present large variations in turbulence levels within the flow, and

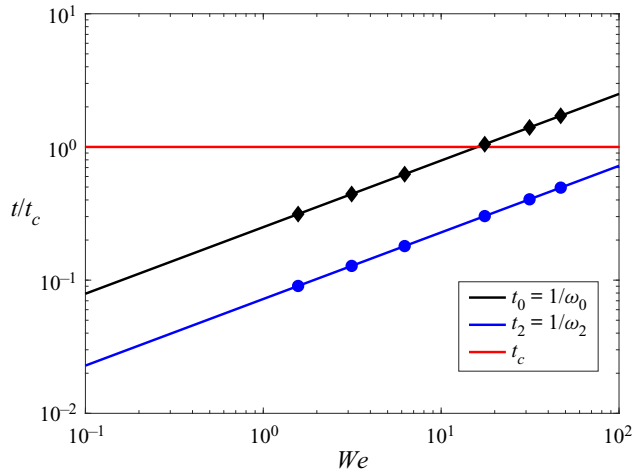


Figure 2. Ratio of characteristic bubble oscillation time scales with the turbulence time scale of the problem as a function of the Weber number. The turbulence time scale is the eddy turnover time at the bubble scale, $t_c = \epsilon^{-1/3} d_0^{2/3}$, the capillary oscillation time is $t_0 = 1/\omega_0 = 1/\sqrt{\gamma/(R_0^3 \rho_\ell)}$ and the time associated to mode 2 is $t_2 = 1/\omega_2 = 1/(2\sqrt{3}\omega_0)$. Symbols correspond to the direct numerical simulation cases in § 3.

Reference	ϵ (m ² s ⁻³)	L (mm)	d (mm)	t_2 (ms)	t_c (ms)
Ruth <i>et al.</i> (2019)	0.5–1	13	2–6	1–6	20–40
Risso & Fabre (1998)	0.1–2	21	4–16	2–40	50–140
Ravelet <i>et al.</i> (2011)	1	10	9	10	50
Martinez-Bazan <i>et al.</i> (1999)	3–100	48–115	3	2	5–35
Vejražka <i>et al.</i> (2018)	0.1–10	4–6	2–6	1–6	15–140
Masuk <i>et al.</i> (2019)	0.16	45–60	2–6	1–6	15–30

Table 1. Estimated experimental time scales and length scales for typical laboratory experiments of bubble deformation and break-up in turbulence. All experiments are made with air bubbles in water. Dissipation rate ϵ and bubble diameter d were directly provided by all authors. Estimates of the integral length scale L were provided by most of the authors, we infer the values for Martinez-Bazan *et al.* (1999) using the usual statistical properties of a turbulent jet (Hussein, Capp & George 1994). The oscillation time is given by $t_2 = 1/2\sqrt{3}\sqrt{\gamma/(R_0^3 \rho_\ell)}$ and the eddy turnover time at the bubble scale is given by $t_c = \epsilon^{-1/3} d_0^{2/3}$.

significant mean shear. A complete discussion on the challenges of experimental systems to study bubble deformation and break-up in homogeneous and isotropic turbulence can be found in Masuk *et al.* (2019). The long-time evolution of bubble deformation depends eventually on the bubble stability. The stability being dependent on the deformation, we postpone the discussion on either the saturation or the break-up time to the end of the direct numerical simulations section (§ 3). The following sections derive asymptotic solutions associated to each temporal regimes.

We note that the compressible mode of deformation for a bubble or diameter $2R$ in a infinite domain of water oscillates at the Minnaert frequency $f_M = 1/(2\pi R)(3\Gamma p_0/\rho_\ell)^{1/2}$ (Minnaert 1933), where Γ is the polytropic coefficient and p_0 the bubble pressure. When considering millimetric air bubbles in water, the Minnaert frequency f_M ranges from [0.5, 10] kHz for sizes in the range [10, 0.5] mm (Deane & Stokes 2002). The acoustic

frequency f_M can be compared with the Lamb oscillation frequency $1/t_2 = \omega_2/(2\pi)$ (Lamb 1995) which is driven by surface tension forces and characteristic of the large deformation and break-up dynamics. For an air bubble in water of millimetric size, this second mode of oscillation $1/t_2$ ranges between $[0.025, 1]$ kHz, so that the ratio $f_M t_2 > 10$ and air compressibility can be neglected when analysing large deformations leading to break-up.

2.5. Early-time solution: linear regime

Starting from a spherical shape at $t = 0$, the first instants verify $\omega_\ell t \ll 1$ and $t \ll t_c$. In this limit we can consider $u_{\ell,m}$ and $\pi_{\ell,m}$ as independent of time, and neglect the surface tension term. From (2.8) and its initial conditions, we get by double integration over time,

$$a_{\ell,m} = u_{\ell,m}t + \frac{C(\ell)}{2R_0}\pi_{\ell,m}t^2. \tag{2.14}$$

The relative influence of each term will depend on the characteristic time scale $2R_0u_{\ell,m}/\pi_{\ell,m}$, of order t_c as it also corresponds to a characteristic time scale of the turbulence at the bubble scale R_0 . For $t \ll t_c$, the pressure contribution is then negligible and the dynamics of each mode $a_{\ell,m}$ reduce to a simple advection by the background flow. Performing an ensemble-average operation yields

$$\langle a_{\ell,m}^2 \rangle = \langle u_{\ell,m}^2 \rangle t^2. \tag{2.15}$$

At short time ($\omega_2 t \ll 1$, $t \ll t_c$), the evolution of $a_{\ell,m}$ is then expected to be independent of surface tension and pressure fluctuations, and this first linear growth regime should hold for all Weber numbers. Note that this limit is similar to the frozen turbulence regime identified for bubble pinch-off in turbulence, in which most of the pinching dynamics occur on a fraction of the eddy turnover time at the scale of the neck (Ruth *et al.* 2019). In both cases, the influence of the turbulent background flow reduces to the set of initial conditions.

Later on, the linear growth regime is limited in time by either the bubble natural oscillations at $1/\omega_2$ or by the correlation time of the turbulent flow t_c , depending on the Weber number as shown in figure 2, or by viscous effects which are not investigated here. For $We \gg 1$, when $t_c < t_2$, the linear regime occurs until $t \approx R_0/u'_{\ell,m} \approx t_c$, which corresponds to $\zeta_\Omega/R_0 \approx 1$, a deformation amplitude sufficient to trigger bubble breaking. Here t_c then coincides with the bubble lifetime, and no later-time evolution is expected.

2.6. Forced oscillator regime

We consider $We < 100$, in which the linear growth is first limited by surface tension ($\omega_2 t_c > 1$). For $t < t_c$, we still consider that $u_{\ell,m}$ and $\pi_{\ell,m}$ are independent of time. We have

$$\ddot{a}_{\ell,m} + \omega_\ell^2 a_{\ell,m} = \dot{u}_{\ell,m} + \frac{C(\ell)}{R_0}\pi_{\ell,m}, \tag{2.16}$$

$$\dot{a}_{\ell,m}(0) = u_{\ell,m}, \tag{2.17}$$

which admits a solution of the form

$$a_{\ell,m} = \frac{u_{\ell,m}}{\omega_\ell} \sin(\omega_\ell t) + \frac{C(\ell)\pi_{\ell,m}}{R_0\omega_\ell^2} (1 - \cos(\omega_\ell t)). \tag{2.18}$$

The evolution of $\langle a_{\ell,m}^2 \rangle$ at short time is given by

$$\langle a_{\ell,m}^2 \rangle = \langle u_{\ell,m}^2 \rangle t^2 + \frac{C(\ell) \langle \pi_{\ell,m} u_{\ell,m} \rangle}{R_0} t^3 - \frac{1}{3} \omega_\ell^2 \langle u_{\ell,m}^2 \rangle t^4 + \frac{C(\ell)^2 \langle \pi_{\ell,m}^2 \rangle t^4}{R_0^2} \frac{1}{4} + O(t^5). \quad (2.19)$$

However, since the terms in $\langle \pi_{\ell,m} u_{\ell,m} \rangle / R_0$ and $\langle \pi_{\ell,m}^2 \rangle / R_0^2$ are respectively of order $\langle u_{\ell,m}^2 \rangle / t_c$ and $\langle u_{\ell,m}^2 \rangle / t_c^2$, their contribution can be neglected for $t \ll t_c$. The first relevant nonlinear term in the range $1/\omega_\ell < t < t_c$ is then the term $-1/3 \langle u_{\ell,m}^2 \rangle t^4$, and the equation for $a_{\ell,m}$ becomes

$$\langle a_{\ell,m}^2 \rangle = \langle u_{\ell,m}^2 \rangle t^2 - \frac{1}{3} \omega_\ell^2 \langle u_{\ell,m}^2 \rangle t^4 + O(t^5), \quad (2.20)$$

which corresponds to a saturation of the linear growth by capillary forces on a time scale $1/\omega_\ell$.

3. Direct numerical simulation of bubble deformation in a turbulent flow

3.1. Numerical methods: the Basilisk flow solver

We perform direct numerical simulations of the three-dimensional, incompressible Navier–Stokes equations, either with a single phase (the turbulence precursor simulation) or with two phases (air bubble and turbulent water) with surface tension, using the free software Basilisk (<http://basilisk.fr/>) (Popinet 2009, 2018). We use a spatial adaptive octree grid allowing us to save computational time while resolving the different length scales of the problem and a momentum conserving scheme. The interface is reconstructed by a sharp geometric volume of fluid method (Popinet 2009, 2018). The solver has been extensively described in recent publications (Popinet 2015; Fuster & Popinet 2018; Popinet 2018; van Hooff *et al.* 2018; Mostert & Deike 2020), and its accuracy has been largely validated on complex multiphase flow, including bubble dynamics (Cano-Lozano *et al.* 2016), bubble bursting (Deike *et al.* 2018; Lai, Eggers & Deike 2018; Berny *et al.* 2020) and wave breaking (Deike, Melville & Popinet 2016; Mostert & Deike 2020; Mostert, Popinet & Deike 2021). We do not consider the effect of gravity in this work. The turbulent two-phase simulations of bubble deformation in turbulence are presented below.

3.2. Preparation: creation of the turbulence and insertion of the bubble

The turbulent flow is generated by adding to the Navier–Stokes equation a volumetric forcing term locally proportional to the velocity field $f\mathbf{u}$, following the approach of Rosales & Meneveau (2005), previously implemented and provided as an example in the Basilisk library (<http://basilisk.fr/src/examples/isotropic.c>). Rosales & Meneveau (2005) showed that such forcing in every point of the real space leads to a well-characterized homogeneous and isotropic turbulent flow with properties similar to those obtained with a spectral code and forcing. Such an approach has also been used by Loisy & Naso (2017) to study rising bubbles in a turbulent flow.

We consider a cubic box of size L with periodic boundary conditions on each side. Adaptive mesh refinement is used on the velocity field, and the maximum level of refinement N allows comparison with a fixed grid resolution having 2^N grid points in each direction. The turbulent flow is generated for increasing resolutions with N going from 6 to 8, corresponding to an equivalent 64^3 to 256^3 grid size on a fixed grid. This resolution is modest but will be increased around the interface when we inject the bubble

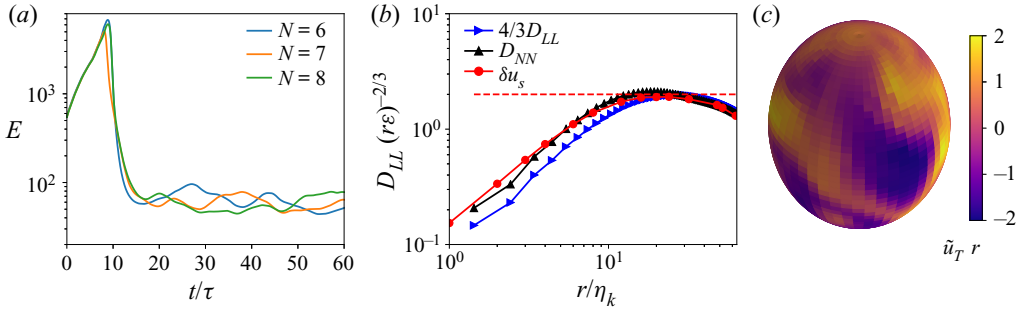


Figure 3. (a) Kinetic energy as a function of time in the precursor simulation for increasing numerical resolution, respectively, level $N = 6, 7$ and 8 . A statistically stationary state is reached after 15τ and numerical convergence is reached for level $N = 7$, with a corresponding turbulent Reynolds number $Re_\lambda = 38$. A bubble will be immersed in this statistically stationary flow, using different initial times as initial conditions. (b) Second-order structure function D_{LL} and D_{NN} in the longitudinal and transverse directions, respectively, compensated by the homogeneous and isotropic turbulence scaling $(r\epsilon)^{-2/3}$ and $D_{LL} = 3/4 D_{NN}$. Kolmogorov theory is superimposed in the red dashed line. (c) Visualization of a snapshot of the instantaneous radial velocity component of the turbulent flow evaluated on a sphere of radius $R/\eta_k = 32$ that a bubble of corresponding size will face.

in the flow, and is chosen to keep the computational cost reasonable for each simulation as we aim to perform a large number of simulations to assess statistical properties of the bubble deformation dynamics.

Figure 3(a) shows the time evolution of the kinetic energy in the precursor simulation, $K = (1/V) \iiint \frac{1}{2} \rho_\ell u(\mathbf{x}, t)^2 dV$. After a short transient, injection and dissipation of energy eventually balances on average and we obtain a statistically stationary, homogeneous and isotropic turbulence. The statistically stationary state is reached after approximately 15 eddy turnover times at the integral scale $\tau = u'^2/\epsilon$, where ϵ is the asymptotic dissipation rate and u' the asymptotic root mean squared velocity. The associated Taylor Reynolds number is $Re_\lambda = (2K/3\mu)\sqrt{15\mu/\epsilon} \approx 38$, which is a typical value for current two-phase simulations of turbulent flow (Loisy & Naso 2017; Elghobashi 2019). Convergence of the statistical properties of the flow with respect to numerical resolution is achieved and is shown with simulations performed at lower maximum refinement. Note that while the flow is statistically stationary and equivalent for the various resolutions, because of the chaotic nature of the flow and the forcing, each realization presents differences one from each other.

Figure 3(b) shows the statistical properties of the turbulent flow once the stationary state is reached. We characterize the fluctuations using the second-order structure functions in the longitudinal $D_{LL}(d)$ and in the transverse direction $D_{NN}(d)$, defined as

$$D_{LL}(d) = \frac{1}{3} \sum_i \langle (u_i(\mathbf{r}, t) - u_i(\mathbf{r} + d\hat{\mathbf{r}}_i, t))^2 \rangle, \quad (3.1)$$

$$D_{NN}(d) = \frac{1}{6} \sum_{i \neq j} \langle (u_i(\mathbf{r}, t) - u_i(\mathbf{r} + d\hat{\mathbf{r}}_j, t))^2 \rangle, \quad (3.2)$$

for homogeneous and isotropic flows, with $\hat{\mathbf{r}}_i$ the unit vector along the i direction. The transverse structure function is compensated by its scaling for a homogeneous and isotropic flow $(d\epsilon)^{2/3}$, and we indeed observe a plateau value close to $C = 2$ (Pope 2000). The relation $D_{LL} = 3/4 D_{NN}$ is also verified by representing the compensated longitudinal structure function $4/3 D_{LL}(d)(d\epsilon)^{-2/3}$. The inertial range is obviously quite limited due

to the relatively coarse resolution, but the turbulent flow at the scale of the bubble to be injected is reasonable, and the bubble radius lies within the inertial range. The quantity of interest for the bubble deformation is the spherical velocity increments, which are defined on a sphere of radius R by

$$\delta u_S(R, \theta, \varphi) = \tilde{\mathbf{u}}(\mathbf{R}, t) \cdot \hat{\mathbf{r}}, \quad (3.3)$$

$$\tilde{\mathbf{u}}(\mathbf{R}) = \mathbf{u} - \frac{1}{4\pi} \iint d\Omega \mathbf{u}(\mathbf{R}, \theta, \varphi, t). \quad (3.4)$$

From homogeneity and isotropy, the statistical properties of $\delta u_S(R)$ shall only depend on r . Figure 3(c) shows the velocity increment δu_S over a sphere of radius $R/\eta_K = 32$, displaying an example of the broad range of forcing scales the bubble sees and feels in the flow. The ensemble-average value $\delta u'_S(R) = \sqrt{\langle (\delta u_S(R))^2 \rangle}$ compensated by $(\epsilon d)^{2/3}$ is represented in red in figure 3(b). We observe $\delta u'_S(R) = D_{NN}(d/2)$ for $Re_\lambda = 38$ in the entire inertial range. The statistical properties of the spherical increment and their link with surface deformations will be further discussed in § 3.

Once the statistically stationary regime is reached, the temporal recording of the velocity field is stored from 20 to 60τ . Different instants are used as initial times for numerical simulations of bubble deformation and break-up. A central sphere of radius R_0 , diameter d_0 and density $\rho_g = 1/850\rho_\ell$ is placed in the periodic box, and the flow in the inner phase is initially set to zero. The bubble diameter is located in the inertial range. For $Re_\lambda = 38$, we have $d_0/\eta_K = 17.6$, $d_0/\lambda = 1.49$ and $d_0/L = 0.13$, where $\eta_K = (\nu^3/\epsilon)^{1/4}$ is the Kolmogorov length scale, λ is the Taylor microscale $\lambda = \sqrt{15\nu u'^2/\epsilon}$ for homogeneous and isotropic turbulence and L is the box size. The level of refinement around the interface is $N = 9$ for the majority of the numerical runs, and convergence tests at level $N = 10$ have been performed. The results on bubble deformation by the turbulent flow presented here are independent of the resolution between refinement levels $N = 9$ and $N = 10$, as shown in the Appendix. These resolutions correspond to 70 and 140 points across the initial bubble diameter, which is comparable to the resolution successfully used to resolve rising motion and path instability of bubbles using the same numerical methods (Cano-Lozano *et al.* 2016).

In a turbulent flow the critical Weber number, or break-up threshold, is defined in a statistical sense; therefore, the probability of breaking does not vanish for a Weber number immediately smaller than $We = We_c$. To determine the critical Weber number, we perform an ensemble of simulations by using different initial times from the turbulence precursor simulation (each precursor typically spaced by $1 - 3t_c$). We do not observe any break-up at $We = 1.5$ while running the simulations up to $20t_c$ for more than 10 runs with different initial conditions. For $We = 3$, we observe break-ups a little over 50 % of the time by $20t_c$ for an ensemble of 35 runs with different initial conditions. It is clear that given the broad lifetime statistics of a bubble in these conditions close to stability, the percentage of cases that do not break might change if the simulations are run for longer times. For $We = 6$, and above, all bubbles break within a few t_c . As such, we consider $We_c = 3$ as the critical Weber number in our configuration and this value is within the variation of experimental measurements discussed in the literature.

Note that we have verified that the order of magnitude of the pressure fluctuations at the bubble surface are too small to induce compressibility effects in the bubble's dynamical response, hence validating the incompressible framework to study millimetric bubbles in water turbulence.

The Weber number, (1.1), is defined considering the temporal average of the turbulence dissipation rate, and we vary the Weber number by changing the surface tension.

Bubble deformation by a turbulent background

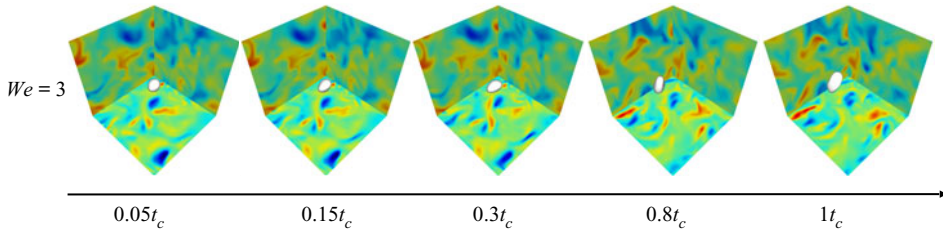


Figure 4. Snapshots of a bubble for one run at $We = 3$, with the interface in white and each background plane showing one component of the velocity. The bubble is injected in the centre of the turbulent domain at $t = 0$ with no velocity and starts to deform quickly. During the first eddy turnover time, no break-up event occurs, but we observe strong and erratic deformations over time as well as advection by the turbulent flow.

Starting from a sphere, we study the growth of the surface deformation until either the saturation of bubble deformation for stable bubbles or the breaking for unstable cases. We perform simulations for a wide range of Weber numbers, $1.5 < We < 45$. The critical Weber number is found at $We_c = 3$, for which about half of the runs do not exhibit bubble break-up after 20τ . We will discuss simulations where, for small Weber numbers ($We \leq 1.5$), no break-up occurs, while for large Weber number, ($We \geq 3$), we will analyse the dynamics before the first break-up. We perform an ensemble of simulations of 10 to 15 runs for each Weber number, using various stored initial conditions from the precursor flow field, leading to a total of about 80 simulations.

Figure 4 shows an example of a bubble evolving in the turbulent flow field in the vicinity of the instability threshold at $We = 3$, during the first eddy turnover time at the bubble scale t_c . The bubble is initially spherical and quickly deforms for $t < 0.5t_c$, and then starts to exhibit erratic oscillations. These deformations do not lead to break-up, and occur together with advection by the turbulent background flow.

3.3. Computing the bubble deformation through a Voronoi decomposition

The interface sampling points r_i are by essence non-uniformly spread, as more points are dynamically added in regions of larger curvature due to the adaptive algorithm. To compute averages accurately over the bubble interface, we then construct a surface scheme using a spherical Voronoi decomposition (Voronoi 1908). The bubble surface is partitioned into regions close to each of the points.

For each region located around the point r_i , we associate a region area A_i and a corresponding solid angle $\Omega_i = A_i/r_i^2$. We evaluate the surface integral of any function f by

$$\frac{1}{4\pi} \iint d\Omega f(\mathbf{r}) = \frac{1}{4\pi} \sum_i f(\mathbf{r}_i) \Omega_i, \quad (3.5)$$

where $\sum_i \Omega_i = 4\pi$. The computation of the region areas A_i and the corresponding solid angles Ω_i is illustrated in figure 5. The Ω_i are computed in three steps. We first project all interface points on the unit sphere (step 1). We then compute the region locations using a spherical Voronoi algorithm based on a robust Delaunay triangulation (Caroli *et al.* 2009) (step 2). The area A_i of each convex polygon is eventually estimated using the shoelace formula (step 3). On the unit sphere, the A_i and Ω_i are identical. An example of our Voronoi decomposition is shown in figure 5(b) on the unit sphere, and in figure 5(c) after projection on the initial bubble shape. The numerical error on the total solid angle $\sum_i \Omega_i$ is less than 0.1 %.

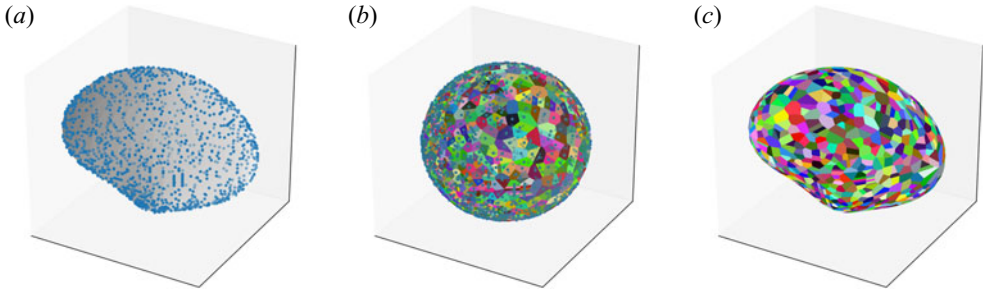


Figure 5. Illustration of the interface tessellation using a spherical Voronoi diagram. (a) Bubble deformed by the turbulent background (one case at $We = 3$, $t/t_c = 0.22$). The output data points are unevenly distributed at the interface. The bubble surface in grey levels has been reconstructed using a two-dimensional spline interpolation. (b) Projection of each point on the unit sphere, and computation of a spherical Voronoi diagram. Each polygon corresponds to the region associated to a single data point. (c) Projection of the Voronoi diagram onto the initial shape bubble using the spline interpolation. The weight of each data point is given by the associated polygon area.

To analyse the interface dynamics using (2.8), we introduce the spherical harmonics $Y_\ell^m(\theta, \varphi)$. The numerical estimate of the harmonic coefficient $a_{\ell,m}$ is obtained by a sum over the interface points \mathbf{r}_i weighted by their local solid angle Ω_i ,

$$a_{\ell,m} = \sum_i \Omega_i \zeta(\mathbf{r}_i) Y_\ell^m(\theta_i, \varphi_i), \quad (3.6)$$

where $(r_i, \theta_i, \varphi_i)$ are the spherical coordinates of \mathbf{r}_i . We have first checked the orthonormal property of the spherical harmonics $(1/4\pi) \iint d\Omega Y_\ell^m \cdot Y_{\ell',m'} = \delta_{\ell,\ell'} \delta_{m,m'}$ for $\ell \in [0, 10]$ and all corresponding m values on a set of 900 points, typical of a surface bubble sampling, and randomly spread on a unit sphere. The typical error is 0.1 % for $\ell < 5$, and increases for higher ℓ values. The harmonic decomposition has been tested on synthetic shapes, i.e. a set of 900 points randomly spread on an interface of known spherical decomposition. The relative error on the harmonic coefficient is about 0.5 % of the largest non-zero harmonic coefficient for $\ell \in [1, 5]$. In practice, since the amplitude decreases rapidly with ℓ , an accurate estimate of the harmonics coefficient is limited to $\ell \leq 5$ for the interface deformation and around $\ell \sim 10$ for the velocity field.

The bubble centre position evolves with time, the interface being advected by the turbulent background flow. To analyse specifically the surface deformations, we look for the centre position \mathbf{r}_c of the bubble frame of reference, for which $a_{1,m} = 0$ for $m \in \{-1, 0, 1\}$, as defined in § 2. The centre position \mathbf{r}_c is computed recursively as follows. At each step, we compute the Voronoi diagram and the associated spherical harmonic functions $Y_{1,m}$ using the regions area A_i . Then, since each function $Y_{1,m}$ presents a symmetry of revolution, a one-dimensional gradient descent on each function is sufficient to find the position centre that minimizes each coefficient $a_{1,m}$. For bubble interfaces with a single-valued radial distance $r_i(\theta, \varphi)$, the gradient descent indeed converges to a centre position \mathbf{r}_c for which the three mode 1 coefficients $a_{1,m}$ vanish.

3.4. Deformation dynamics for stable conditions: bubble deformation and temporal evolution of spherical modes

We first describe the temporal evolution of the coefficients $a_{\ell,m}$ for a single run at $We = 3$, as an illustration of the analysis performed on each simulation. Several modes $a_{\ell,m}$ of the

same ℓ and different m values are associated to the same oscillation frequency (see (2.8)); therefore, we introduce the global coefficient a_ℓ describing the energy contained in each mode ℓ , defined by

$$a_\ell^2 = \sum_{m=-\ell}^{\ell} a_{\ell,m}^2, \quad (3.7)$$

where a_ℓ is then positive by convention. The global surface deformation is obtained by a sum over all modes ℓ . We recall the expression of the root mean squared deformation ζ_Ω : $\zeta_\Omega^2(t) = \sum_{\ell=2}^{+\infty} \sum_{m=-\ell}^{\ell} a_{\ell,m}^2(t)$. Figure 6(a) shows the time evolution of ζ_Ω/R_0 together with the total amplitude of mode 2, a_2/R_0 . We observe a rapid linear rise, consistent with the prediction for $t \ll t_2, t_c$, before oscillations and saturation of the total deformation around $\zeta_\Omega/R_0 \approx 0.15$. As shown in the figure, most of the deformation comes from the mode $\ell = 2$. This first observation is in agreement with various experimental studies on large bubbles immersed in a turbulent flow, which have reported the dominance of mode 2 deformation in bubble dynamics (Risso & Fabre 1998; Ravelet *et al.* 2011). In practice, a sum over the first three modes $\ell = 2, 3, 4$ estimates the amplitude deformation ζ_Ω within less than 2% error as long as $\zeta_\Omega/R_0 < 1$ for all cases. It confirms the predominance of the first modes of oscillation, and validates the spherical decomposition approach. In the following, we focus on the modes $\ell = 2, 3$ and 4 which contribute mostly to the surface deformation.

Figure 6(b) shows the temporal evolution of a_ℓ^2 for the first few spherical harmonics $\ell \in [1, 4]$ for a single run. The modes $\ell = 1$ have zero amplitude from the choice of the centre position, and the modes $\ell = 2$ dominate the surface energy deformation. The energy contained in modes $\ell = 2$ oscillates with time, at a frequency close to $2\omega_2$ and the energies in the higher-order modes $\ell = 3, 4$ and 5 remain smaller at all times. Figure 6(c) shows the temporal evolution of each individual harmonic coefficient $a_{2,m}$ for different m components. All five coefficients appear to oscillate with comparable amplitude and with frequencies close to ω_2 .

3.5. Deformation dynamics for increasing Weber number and unstable conditions

For one particular configuration of the turbulent flow, we investigate the role of the Weber number on the deformation by changing only the value of the surface tension. Figure 7 shows snapshots of the bubbles for increasing Weber numbers, $We = 3, 6$ and 15, for the same initial turbulent conditions. For all cases, we observe early growth of surface deformation, while the turbulent background flow stays identical for all runs and independent of surface tension, validating the no-feedback hypothesis introduced in § 2. For all We , the short time deformation under the same turbulence conditions appears identical, in agreement with the theoretical description of the linear regime for $t \ll t_c$. For stable conditions (here $We = 3$), the deformation rapidly saturates as previously described. For unstable conditions (here $We = 6$ and 15), the deformations eventually lead to break-up at various times. The highest Weber number ($We = 15$) displays a break-up event relatively early at $t/t_c \approx 0.8$, while for conditions closer to the stability threshold, break-up occurs at $t/t_c > 1$.

A quantitative description of the Weber number influence for one particular run is given in figure 8. We compute the total deformation ζ_Ω starting from the same initial condition of the flow configuration, and increasing values of the Weber number $We = 1.5, 3, 6, 15, 30$ and 45. Figure 8 shows the deformation ζ_Ω/R_0 as a function of time t/t_c . We observe a universal rapid linear growth, followed by a saturation that depends on

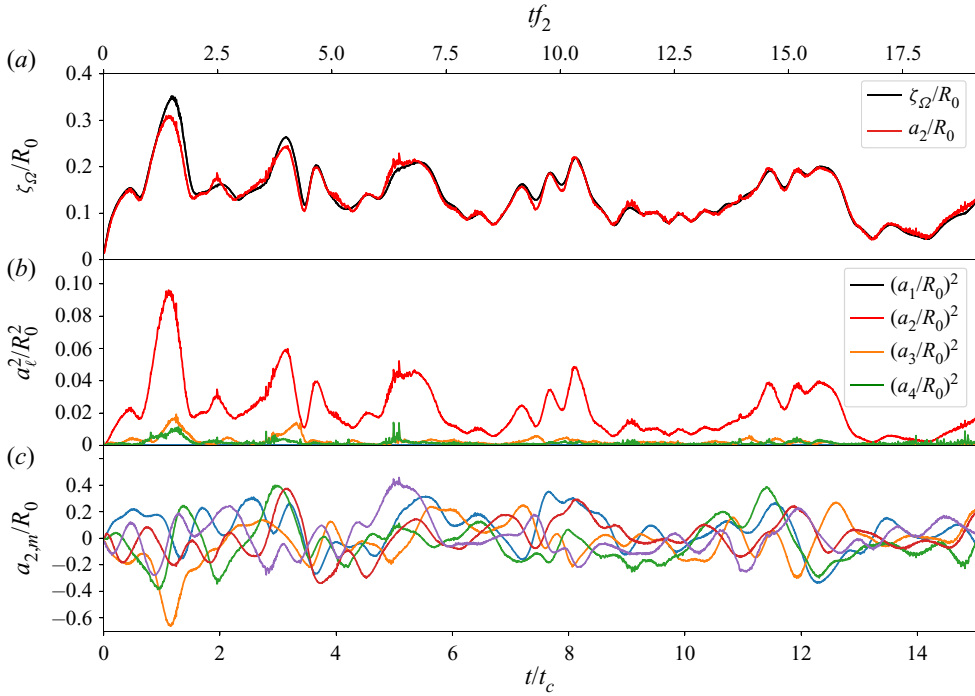


Figure 6. (a) Total deformation ζ_Ω/R_0 as a function of time, together with the root mean square (r.m.s.) amplitude of the mode 2 oscillations. (b) Energy $a_\ell^2 = \sum_{m=-\ell}^{\ell} a_{\ell,m}^2$ of the spherical harmonics for modes $\ell = 1$ to $\ell = 4$ for one run at $We = 3$. Mode 1 energy vanishes by definition. Mode 2 appears as the most energetic mode, in agreement with experimental literature, with oscillation close to $f_2 = \omega_2/(2\pi)$. As ℓ increases, the energy contained decreases sharply. (c) Temporal evolution of the amplitude coefficients $a_{2,m}$ for mode $\ell = 2$, and $m = -2$ to $m = +2$. All modes m oscillate with similar amplitude and frequency.

the Weber number. The rapid linear growth is independent of the Weber number for $t/t_c < 0.1$, as expected from (2.14). As time passes, the curves diverge from each other, and the lower Weber number curves exhibit earlier sublinear growth. The saturation leads to long-time oscillations at the low Weber numbers, namely $We = 1.5, 3$ and 6 during several eddy turnover times, with increasing amplitude as the Weber number increases. For larger Weber numbers (here $We = 15$ and 45), the bubble experiences break-up during the first eddy turnover time, when surface deformation reaches $\zeta_\Omega/R_0 \approx 0.74$. Note that the deformation at break-up is estimated from a fit of the bubble interface by an ellipsoidal shape at the break-up time, as the Voronoi decomposition fails at large deformation, significantly before break-up.

3.6. Ensemble-averaged deformations at one Weber number: linear growth and saturated regime

To obtain ensemble-average quantities, we analysed between 10 to 15 runs for each Weber number, starting from different turbulent flow configurations, which are obtained from different times of the precursor simulations. For each run, we perform the analysis described above, from the Voronoi decomposition to the computation of the surface deformation ζ_Ω and the first harmonics coefficients a_2, a_3 and a_4 .

Figure 9(a) shows the temporal evolution of each individual realisation of ζ_Ω/R_0 performed at $We = 3$, as a function of the dimensionless time t/t_c . The ensemble average

Bubble deformation by a turbulent background

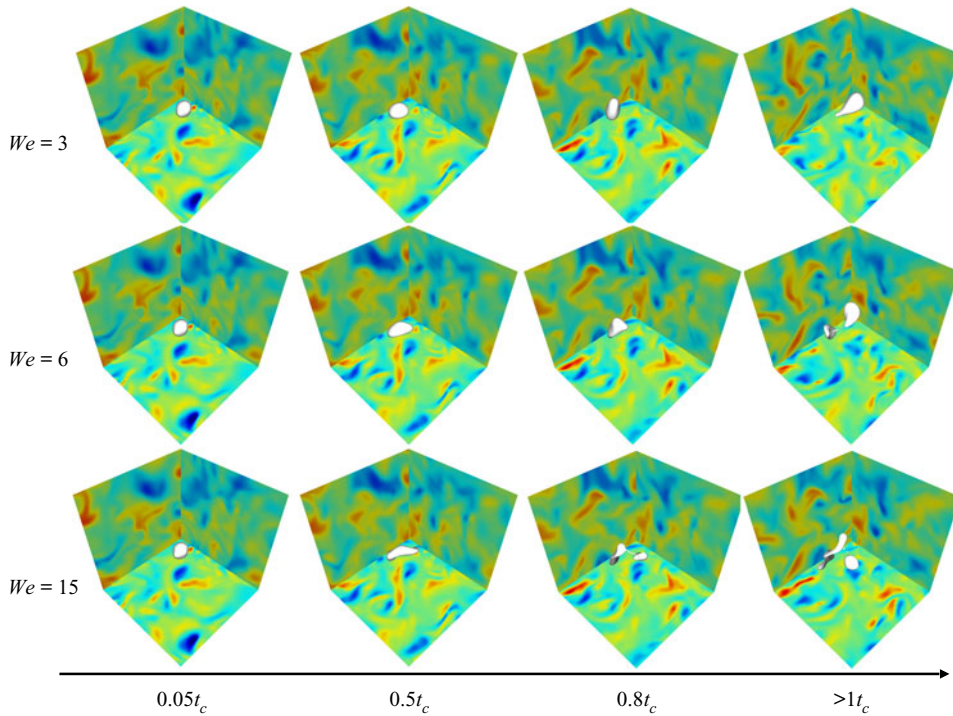


Figure 7. Bubble deformation and break-up as time progresses for the same initial conditions but increasing Weber number. Time increases from left to right while We increases from top to bottom. At $We = 3$, this particular condition does not lead to break-up. At $We = 6$, break-up occurs for $t/t_c \approx 1.5$, while break-up occurs earlier for $We = 15$ at $t/t_c \approx 0.8$. The initial stage of deformation for $t < 0.5t_c$ appears very similar at all Weber numbers.

$\langle \zeta_\Omega \rangle / R_0$ is superimposed in black, and follows a linear increase, as predicted by (2.15). The mode 2 amplitude a_2 / R_0 is superimposed in figure 9(a) (\square , red), confirming in a statistical sense the predominance of the mode 2 oscillations. The modes a_2 / R_0 and a_3 / R_0 follow the same trend, as shown in figures 9(b) and 9(c), each coloured curve being an individual realisation. Again, at short time the linear regime predicted by (2.15) is observed.

We observe a transition to a sublinear regime for $\langle \zeta_\Omega \rangle$, $\langle a_2 \rangle$ and $\langle a_3 \rangle$ around $0.1 < t < 0.3$. This transition is well described by the theoretical expression derived in § 2 (2.20), i.e. $\propto t\sqrt{1 - (\kappa t)^2}$, with $\kappa = \omega_2 / \sqrt{3}$ for $\langle \zeta_\Omega \rangle$ or $\langle a_2 \rangle$, and $\kappa = \omega_3 / \sqrt{3}$ for $\langle a_3 \rangle$. The prefactor is related to the turbulence velocity field statistics $u_{\ell,m}$, which will be evaluated in an upcoming section. In order to evaluate the saturation with time, we describe the temporal evolution of $\langle \zeta_\Omega \rangle$, $\langle a_2 \rangle$ and $\langle a_3 \rangle$ by the empirical expression $a_\ell^\infty (1 - e^{-t/t_{sat}})$ with two fit parameters a_ℓ^∞ and t_{sat} . The early-time evolution is proportional to a_ℓ^∞ / t_{sat} , while the characteristic time of saturation is given by t_{sat} . Eventually, we perform for each ensemble-average mode $\langle a_\ell \rangle$, a linear fit $a_\ell = s_\ell t$ in the early-time evolution ($t < t_{sat}/2$) by a simple linear model, which gives an accurate measure of the growth velocity s_ℓ .

3.7. Ensemble-averaged deformations for increasing Weber number

Figure 10 summarizes the surface deformation growth for increasing Weber number. Figure 10(a) shows the evolution of $\langle \zeta_\Omega \rangle$ averaged over at least 10 runs by Weber number,

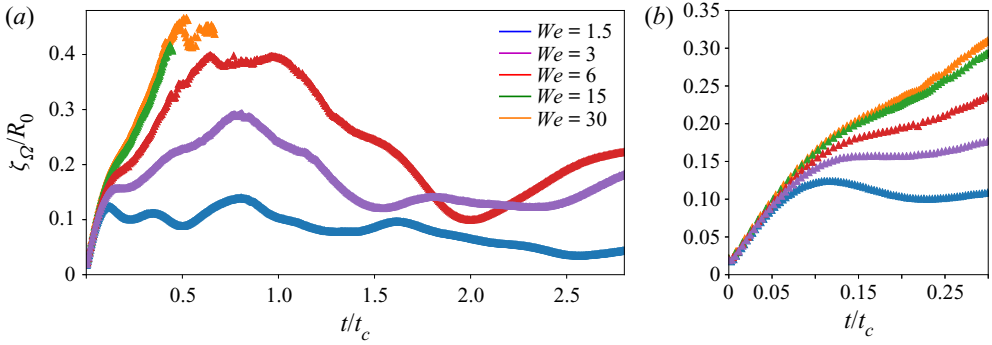


Figure 8. (a) Root mean square surface deformation ζ_{Ω} as a function of time t/t_c for the same initial turbulent flow condition and increasing Weber number $We = 1.5, 3, 6, 15, 30$. (b) Zoom-in on the early stage dynamics. For $t/t_c < 0.1$, a universal linear increase of the deformation is observed at all Weber numbers. Earlier saturation time is reached for higher surface tension forces (lower We), leading to lower values of the saturated deformation amplitude.

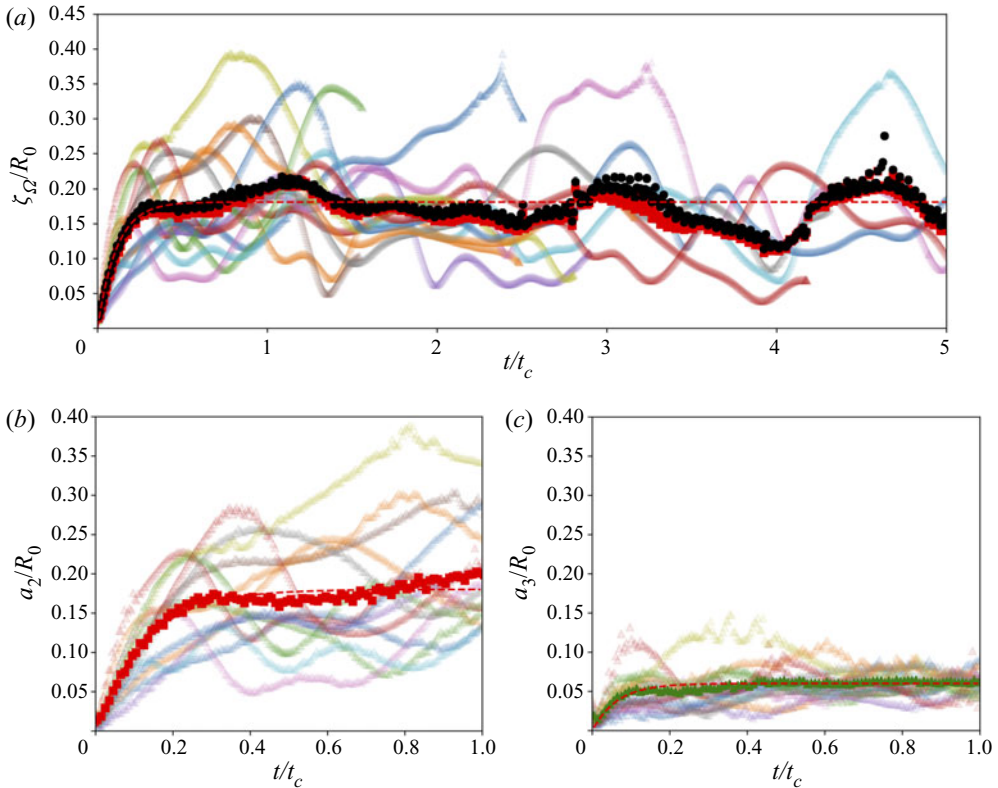


Figure 9. (a) Individual realisations of ζ_{Ω} at $We = 3$, as a function of the dimensionless time t/t_c in transparent colours. Ensemble average $\langle \zeta_{\Omega} \rangle$ of the surface deformation is superimposed (black full symbols), together with the ensemble-average mode 2 amplitude (red full symbol). (b) Coefficient a_2 as a function of dimensionless time t/t_c for $We = 3$ (individual realisations in transparent colours). Ensemble average $\langle a_2 \rangle$ is superimposed (full red symbol). Fit by $A(1 - e^{-t/t_{sat}})$ of the ensemble average a_2 in shown by the dashed lines. (c) Coefficient a_3 as a function of dimensionless time t/t_c for $We = 3$ and the equivalent exponential fit (individual realisations are transparent colours and the green full triangle is ensemble average $\langle a_3 \rangle$).

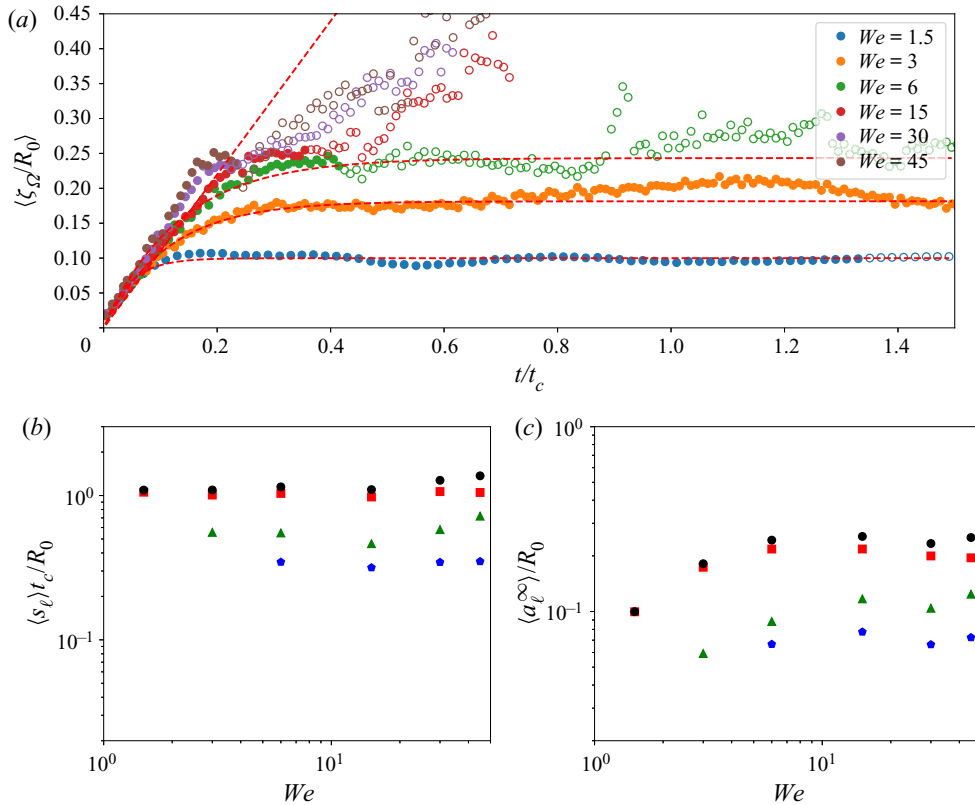


Figure 10. (a) Ensemble-averaged deformation $\langle \zeta_\Omega \rangle$ as a function of time for increasing Weber number. For the lower We , a fit by $A(1 - e^{-t/t_{sat}})$ captures the transition from linear growth to saturation, with saturation values increasing with We . Open symbols are used once half of the bubbles in the ensemble have broken. (b) Slope at the origin as a function of the Weber number for $\langle \zeta_\Omega \rangle$, $\langle a_2 \rangle$, $\langle a_3 \rangle$, $\langle a_4 \rangle$. The slope at the origin for $\langle \zeta_\Omega \rangle$ is independent of We . (c) Amplitude of saturation of the global deformation and modes as a function of We .

as a function of the Weber number. The evolution is shown in solid symbols until half of the bubbles have broken, and in open symbols later. At early time, we show the existence of a universal regime, with a linear increase in time of the deformations independent of the Weber number. Similar results are observed when considering the spherical harmonics amplitude $\langle a_2 \rangle$, $\langle a_3 \rangle$ and $\langle a_4 \rangle$. The dimensionless growth velocity $s_\ell t_c/R_0$ at short time, obtained from the linear fits, is shown in figure 10(b) as a function of the Weber number for $\langle \zeta_\Omega \rangle/R_0$ (\circ), $\langle a_2 \rangle$ (red square), $\langle a_3 \rangle$ (green triangle) and $\langle a_4 \rangle$ (blue pentagon). For the low Weber numbers $We = 1.5$ and $We = 3$, only the modes that are significantly above the noise level have been represented, excluding modes 3 and 4 at $We = 1.5$, and mode 4 at $We = 3$. The growth velocity s_ℓ depends on the mode ℓ , but is independent of Weber number, as expected from (2.8) and (2.15).

The departure from linear growth that occurs at a time increasing with Weber number is compatible with the prediction given the second mode reduced period t_2 . Eventually, the saturation can be measured using the exponential fit for the lowest Weber number ($We = 1.5, 3$ and 6) where a saturation is clearly visible. For higher Weber numbers, we consider the value of the linear fitting model, evaluated at the time of the first break-up. The saturation time for $We < 10$ and the earliest break-up value for $We > 10$ is shown in figure 10(c). We observe a continuous growth with Weber number, premising the likelihood of

bubble break-up. At higher Weber numbers, we also remark that the relative amplitudes of modes 3 and 4 are increasing for both the growth velocity s_ℓ and the saturation a_ℓ^∞ . At high Weber numbers, the higher-order modes of deformation in the global dynamics become more important and are likely to influence the break-up geometry that the bubble will experience.

Note that treating the saturation at an intermediate Weber number would require considering the role of nonlinear and viscous effects. Note also that for $\zeta_\Omega/R_0 > 0.25$, a significant part of the bubbles have broken, and the mean deformation observed when considering all break-up events is $\zeta_\Omega/R_0 \approx 0.74$, which is compatible with the observations on areas of deformation at break-up made by Risso & Fabre (1998).

Having access to the full velocity flow, we can now relate the surface deformation growth parametrized by a_ℓ and s_ℓ to the statistics of the surrounding turbulent flow.

3.8. Statistics of velocity increments on a sphere predict the linear growth of deformation

From the theory developed in § 2, the prefactor of the linear growth regime of the spherical harmonics mode amplitude shall be related to the statistics of the turbulent flow. Indeed, the growth of the spherical harmonics coefficients $a_{\ell,m}$ is linked to their counterpart in the turbulent fluctuations, $u_{\ell,m}$ and $\pi_{\ell,m}$ in (2.8), (2.15) and (2.20). It bears significant importance from a practical point of view, as measuring velocity statistics in an experimental or natural turbulent flow is relatively accessible while measuring deformation properties on a bubble interface is much more challenging. We recall the description of the spherical increments, δu_S , which can be decomposed in the spherical harmonics base, $\delta u_S = \sum_{\ell=2}^{+\infty} \sum_{m=-\ell}^{\ell} u_{\ell,m} Y_\ell^m(\theta, \varphi)$, where $u_{\ell,m}$ depends on the radius r of the sphere.

Using the velocity flow in the direct numerical simulations, we computed the ensemble average $\langle u_\ell \rangle$ of the harmonic coefficients of $\delta u_S(r)$ for $r = R_0$, using the same procedure as for the a_ℓ . The dimensionless coefficients $\langle u_\ell \rangle t_c/R_0$ are shown in figure 11(a), and in table 2 as red stars for $\ell = 2, 3$ and 4 and correspond to the intensity of velocity fluctuations at the bubble scale for specific modes ℓ . The coefficients $s_\ell t_c/R_0$ obtained from the processing of surface deformations are superimposed in black circles and correspond to the intensity of deformations of the bubbles for the corresponding modes ℓ . For modes $\ell = 2, 3$ and 4, we find a quantitative agreement between $\langle a_{\ell,m} \rangle$ and $\langle u_{\ell,m} \rangle t$, as expected from § 2, (2.15). For $\ell = 4$, we observe a slight difference for $\ell = 4$ with $s_4 > u_4$, which can be attributed to the limit of resolution of the harmonics coefficient computation on the bubble deformation for higher ℓ values.

Beyond the equality of the ensemble-average values, the prediction made in § 2 shall be valid for each individual realisation. This equality can be used to infer the full statistics of $a_{\ell,m}$ at short time, using the statistics of the $u_{\ell,m}$ in the background flow.

Figure 11(b) shows the probability density function (p.d.f.) of the dimensionless mode 2 $u_2 t_c/R_0$ at the bubble scale R_0 . In contrary to the two-points velocity increment $D_{LL}(R_0)$, the p.d.f. of u_2 in the inertial range does not exhibit large tails, and 95 % of u_2 values lie in the range $[0.5\langle u_2 \rangle, 2\langle u_2 \rangle]$. The difference between the large tails of the p.d.f. of D_{LL} at $d/\lambda = 1.5$ and the short tails of u_2 can be attributed to the spatial average operation on the sphere, which smoothes out all the intermittent structures at a scale smaller than the bubble, and suggests that the flow intermittency has a limited influence on the bubble deformation in the inertial range. Considering a positive definite quantity, a fit of the p.d.f. by a Γ -distribution of expression $f(x, k, p) = x^{k-1} e^{-x/p} / \Gamma(k) p^k$ gives $k = 7.5$ and $p = 0.135$.

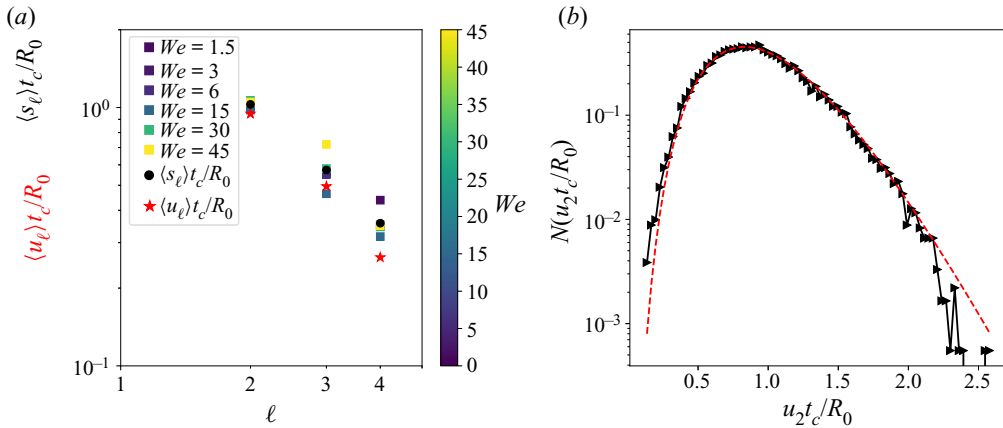


Figure 11. (a) Ensemble average of the spherical harmonics growth rate $\langle s_\ell \rangle R_0 / t_c$ for $\ell = 2, 3$ and 4 , together with the corresponding spherical harmonics flow coefficient $\langle u_\ell \rangle t_c / R_0$ of the turbulent velocity fluctuations at the bubble scale, shown as red stars. Black circles are $\langle s_\ell \rangle t_c / R_0$ averaged for all We , while the coloured squares correspond to the Weber number scale (see colourbar). The theoretical prediction $a_\ell = u_\ell t$ from § 2 is well verified, with velocity fluctuations providing a quantitative prediction of the bubble deformation. The interface deformation statistics at early times can thus be extracted from velocity fluctuations at the bubble scale. (b) Probability distribution of the velocity fluctuations $\langle u_2 \rangle$ corresponding to the statistics of velocity fluctuations on the bubble sphere responsible for mode 2 deformation. A fit by a Γ -distribution of expression $f(x, k, p) = x^{k-1} e^{-x/p} / \Gamma(k)p^k$ is superimposed (red dashed line) with $k = 7.5$ and $p = 0.135$.

$We =$	1.5	3	6	15	30	45	$Re_\lambda =$	38
$\langle s_2 \rangle R_0 / t_c$	1.06	1	1.03	0.93	0.98	0.95	$\langle u_2 \rangle t_c / R_0$	0.95
$\langle s_3 \rangle R_0 / t_c$	0.56	0.55	0.54	0.44	0.51	0.64	$\langle u_3 \rangle t_c / R_0$	0.50
$\langle s_4 \rangle R_0 / t_c$	0.44	0.35	0.34	0.31	0.33	0.35	$\langle u_4 \rangle t_c / R_0$	0.26
$s_2' R_0 / t_c$	0.41	0.36	0.33	0.32	0.33	0.27	$u_2' t_c / R_0$	0.34
$s_3' R_0 / t_c$	0.23	0.24	0.23	0.15	0.23	0.27	$u_3' t_c / R_0$	0.17
$s_4' R_0 / t_c$	0.08	0.06	0.08	0.08	0.10	0.09	$u_4' t_c / R_0$	0.09

Table 2. Values of the coefficients shown in figures 10 and 11. Ensemble average of spherical harmonics growth rate $\langle s_\ell \rangle R_0 / t_c$ for $\ell = 2, 3$ and 4 . The corresponding spherical harmonics amplitude $\langle u_\ell \rangle t_c / R_0$ of the turbulent velocity fluctuations at the bubble scale is also provided, computed for $Re_\lambda = 38$.

4. Implications for bubble lifetime statistics

Given the linear growth of deformation with time and a growth rate given by the mode u_2 , the p.d.f. of u_2 can be used to evaluate the bubble lifetime distribution at high Weber number when surface tension becomes negligible. In the limit of inertial break-up, with correlated velocity fluctuations, the distribution of lifetime $N(T/t_c)$ at high Weber number is given by

$$N(T/t_c) = N\left(\frac{\langle \zeta_c \rangle}{u_2 t_c}\right), \tag{4.1}$$

where $\langle \zeta_c \rangle$ is the average critical deformation of ζ_Ω at break-up. Here ζ_c cannot be computed from the Voronoi decomposition of the interface, since the radius becomes multivalued at high deformation. To evaluate the critical deformation ζ_c , we approximate the shape at break-up by an ellipsoid of the same volume as the initial bubble and whose longest axis corresponds to the maximum distance between two points on the

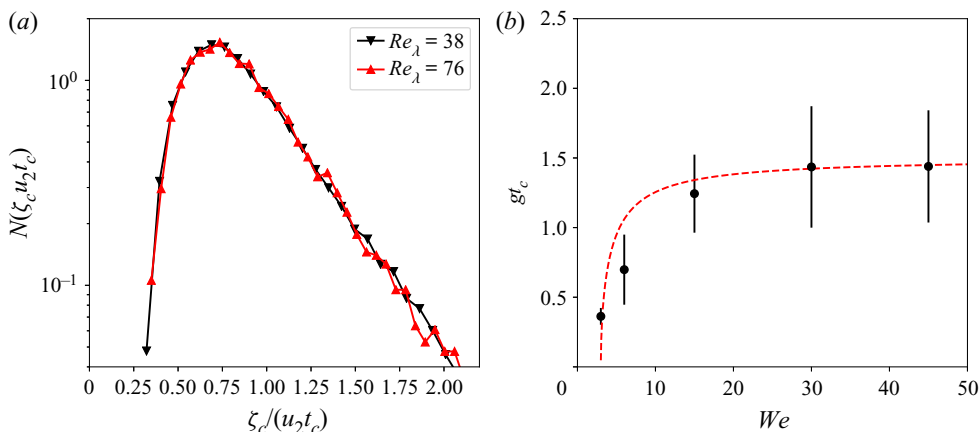


Figure 12. (a) Estimated probability distribution function of bubble lifetime in the limit of large Weber number, obtained from $N(T/t_c) = N(\zeta_c/u_2 t_c)$ (4.1), and valid at high Weber number, i.e. $We \gg 30$, using $\zeta_c = 0.74R_0$. Mean and r.m.s. values are given in table 3. (b) Inverse of the bubble lifetime t_c/T , and its standard deviation, similar to the bubble break-up frequency, as a function of the Weber number. The mean values for 10 to 20 simulations for each Weber number are used, and the error-bar corresponds to the standard deviation in the lifetime. Dashed line corresponds to the model proposed by Martinez-Bazan *et al.* (1999) and Martinez-Bazan *et al.* (2010), $t_c/T \propto \sqrt{1 - We_c/We}$. At high Weber number, the bubble lifetime can be predicted from the turbulence statistics, and given by $\zeta_c/u_2 t_c$.

bubble interface. From the large-Weber-number data ($We \geq 15$) we find that $\langle \zeta_c \rangle = 0.74$. Figure 12(a) shows the distribution $N(T/t_c)$ obtained from (4.1) for a bubble of size $d_0/\lambda = 1.5$ using the statistics of the mode u_2 of the harmonic decomposition of u_T for a Taylor Reynolds number $Re_\lambda = 38$ (the turbulence considered in the present paper). The lower lifetime bound is $0.1t_c$, while the distribution shows exponential tails for large values of the bubble lifetime. We also compute the same predicted lifetime statistics for a turbulent flow obtained similarly but with higher Reynolds number, $Re_\lambda = 76$, and test values of $d_0/\lambda = 1.5$ (red line on figure 12a) and $d_0/\lambda = 3$ and observe only little changes in the distribution. This suggests that the lifetime statistics are fairly insensitive to the Reynolds number for bubbles within the inertial range ($d_0/\lambda > 1$).

The average bubble lifetime can be computed from the numerical runs for each Weber number from the break-up time of the initial bubble. Figure 12(b) shows the inverse of the bubble lifetime t_c/T , similar to the break-up frequency introduced in the literature, for increasing Weber number. The errorbars correspond to the r.m.s. values T_{rms}/t_c . We observe that the bubble lifetime decreases with Weber number, and reaches a value independent of Weber number for $We \gg We_c$, here above $We = 30$. We observe that our data can be reasonably well described by the model proposed by Martinez-Bazan *et al.* (1999) and Martinez-Bazan *et al.* (2010) (dashed line), $t_c/T = C_g \sqrt{1 - We_c/We}$, with the saturation value at high Weber number being the only adjusted parameter. We use $We_c = 3$ and $C_g = 1.5$ is fitted to our numerical data, whereas Martinez-Bazan *et al.* (1999) and Martinez-Bazan *et al.* (2010) used $C_g = 0.673$ and $We_c = 1$ to fit their data.

Table 3 summarizes the bubble lifetime and the estimated lifetime from velocity statistics. The mean and standard deviation values of the inferred lifetime from the turbulence statistics can be compared with the bubble lifetime obtained from the direct numerical simulations for ensembles of 20 to 45 simulations. We observe excellent agreement between the inferred and simulated mean lifetime, as well as for the r.m.s. value of the distribution, considering a constant break-up threshold of $\zeta_c = 0.74R_0$, inferred

	$We = 3$	$We = 6$	$We = 15$	$We = 30$	$We = 45$	$Re_\lambda = 38$
No of elements	45 (13)	39 (14)	20 (8)	20 (7)	20 (7)	
T/t_c	3.01	2.15	1.06	0.90	0.88	$\langle \zeta_c \rangle / (\langle u_2 \rangle t_c) = 0.91$
T_{rms}/t_c	0.86	1.18	0.65	0.45	0.40	$\langle \zeta_c \rangle / (u_2' t_c) = 0.41$
$\langle \zeta_c \rangle / R_0$	0.25	0.5	0.68	0.85	0.69	

Table 3. Bubble lifetime obtained as a function of Weber number, obtained from the direct numerical simulations and from the turbulence statistics. The mean T and r.m.s. T_{rms} values of the bubble lifetime obtained from ensembles of 20 to 45 simulations at increasing Weber number (number of elements indicated in first row). We also provide the computed mean deformation at break-up $\langle \zeta \rangle$. The number in parentheses corresponds to the number of elements used to compute the deformation at break-up ζ_c from the bubble deformation simulations. On the right of the table, we show the predicted mean and r.m.s. lifetime from the turbulence statistics, $\zeta_c / (\langle u_2 \rangle t_c)$, for a constant deformation threshold $\zeta_c / R_0 = 0.74$, for $Re_\lambda = 38$. Excellent agreement between the numerical values and those predicted by the turbulence statistics is observed at high Weber number.

from the bubble deformation at break-up for high-Weber-number cases ($We \geq 15$). The full distribution $N(T/t_c) = N(\langle \zeta_c \rangle / (u_2 t_c))$ could hence be a good estimate of bubble lifetime statistics in the limit of high Weber number.

5. Conclusion

We have presented a theoretical framework for bubble deformation in a turbulent flow by performing a spherical harmonics decomposition of the bubble deformation and deriving a general forced oscillator equation for these spherical harmonics modes, where each mode is forced by the corresponding turbulent fluctuations mode. We identify various regimes in the time evolution of the deformation, in particular, a short time scale regime where deformations grow linearly with time, the prefactor being given by the strength of the turbulent flow.

We perform direct numerical simulations of bubbles evolving in homogeneous and isotropic turbulent flow at increasing Weber number and verify the theoretical predictions. We observe the linear regime of deformation growth for individual events and ensemble-averaged quantities and show that the prefactor of the linear growth is indeed given by the statistics of the turbulence deformation at the bubble scale. We observe in the simulations that the level of deformation saturates, with a saturation time and level of saturation that depends on the Weber number, with lower Weber numbers saturating earlier and at lower deformation. At low to intermediate Weber numbers, eigenmode 2 dominates the deformation. At lower Weber numbers, a much broader lifetime distribution is observed, with break-up that can occur at much later time, as multiple eddies participate in the deformation and break-up, as described in Risso & Fabre (1998). The broad lifetime distribution can be interpreted as a consequence of a stochastic process with a threshold, which gives rise to long oscillation before a fluctuation of higher amplitude leads to break-up. Further stochastic analysis of the surface deformation fluctuations around the average saturation, accounting for nonlinear and viscous effects, could provide a quantitative prediction of the lifetime distribution at intermediate Weber numbers.

At high Weber numbers, break-up occurs within a single eddy turnover time, and close to the linear regime of deformation. These findings have significant implications: the ability to predict bubble deformation and break-up time from the turbulence statistics is now possible by extracting the turbulence statistics and computing the spherical harmonics

decomposition of the corresponding modes 2 and 3. According to our theory and as shown in the final section, the statistics of such modes directly provide the bubble lifetime, if one assumes a maximum deformation threshold. Our data typically suggest $\zeta_{\Omega}/R_0 \approx 0.74$. The deformation also shows significant increase of higher frequency modes, which could be related at high Weber numbers to the appearance of much smaller child bubbles. A more elaborate model would require a better estimate of the deformation statistics at break-up.

Experimental work probing the full three-dimensional turbulence, while challenging, could further test these results on bubble deformation, bubble lifetime and break-up in turbulence. Another prospect involves simulations at higher turbulent Reynolds numbers investigating the roles of the ratio between the turbulent length scales and the bubble deformation dynamics, as well as the local coupling between the turbulent flow in the dense phase and the bubble deformations. Similarly, this numerical framework could be used to explore the child bubble size distribution resulting from bubble break-up (see Rivière *et al.* 2021) and its relationship with the turbulence statistics.

Acknowledgements. We are indebted to an anonymous reviewer for his comments on the presentation of the theoretical section in an earlier version of the paper. We thank S. Popinet for scientific discussions and development of the Basilisk package. We thank the three anonymous reviewers whose comments have helped improve the quality of the manuscript.

Funding. This work was supported by the NSF CAREER award 1844932 to L.D., and the American Chemical Society Petroleum Research Fund Grant 59697-DN19 to L.D. A.R. was supported by an International Fund grant from Princeton University to L.D. S.P. and A.R. were supported by the Labex ENS-ICFP. We would like to acknowledge high-performance computing support from Cheyenne (doi:10.5065/D6RX99HX) provided by NCAR's Computational and Information Systems Laboratory, sponsored by the National Science Foundation. Computations were also performed on the Princeton supercomputer Tiger2, as well as on Stampede, through XSEDE allocations to L.D. and W.M., XSEDE is an NSF funded program 1548562.

Declaration of interests. The authors report no conflict of interest.

Author ORCID.

- ① Stéphane Perrard <https://orcid.org/0000-0002-9315-2892>;
- ① Aliénor Rivière <https://orcid.org/0000-0002-5658-0759>;
- ① Wouter Mostert <https://orcid.org/0000-0001-6251-4136>;
- ① Luc Deike <https://orcid.org/0000-0002-4644-9909>.

Appendix. Convergence test

We present in figure 13 a convergence test on the interface resolution by running simulations for maximum interface refinement levels $N = 9$ and $N = 10$, using the same precursor simulation. As discussed in § 3, these resolutions correspond to 70 and 140 grid points per diameter, while the resolution of the turbulent flow remains the same, and correspond to the $Re_{\lambda} = 38$ flow with a velocity refinement of level 7. The interface deformation ζ_{Ω} as a function of time is shown in figure 12, for increasing Weber number. We observe quasi-identical results between the maximum levels 9 and 10, for all cases, for times of the order of the eddy turnover time. This shows that the interface deformation is correctly resolved at the chosen resolution, and the results presented in the paper are independent of numerical resolution. It is important to remember that the increase in resolution here only applies to the interface resolution, while the resolution on the turbulent velocity field remains the same. However, we have independently verified that the statistical properties of the turbulent flow are also converged at the resolution we are using (see figure 3).

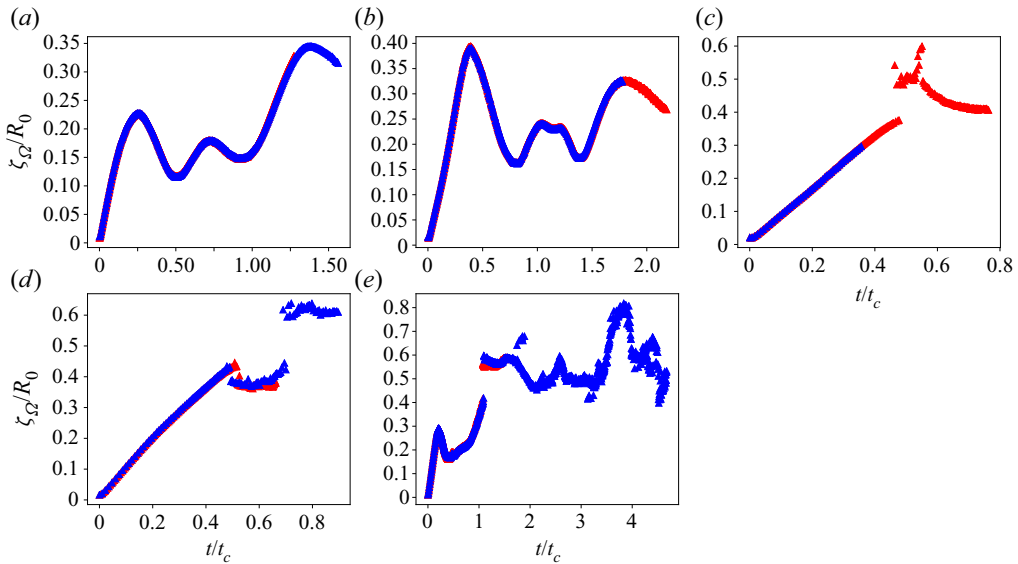


Figure 13. Convergence test on ζ_Ω as a function of dimensionless time t/t_c for $We = 3, 6, 15, 30, 45$. Level $N = 9$ (blue) and level $N = 10$ (red). Excellent convergence agreement is observed between the two numerical resolutions.

REFERENCES

- ANDERSSON, R. & ANDERSSON, B. 2006 On the breakup of fluid particles in turbulent flows. *AICHE J.* **52** (6), 2020–2030.
- BALACHANDAR, S. & EATON, J.K. 2010 Turbulent dispersed multiphase flow. *Annu. Rev. Fluid Mech.* **42**, 111–133.
- BERNY, A., DEIKE, L., SÉON, T. & POPINET, S. 2020 Role of all jet drops in mass transfer from bursting bubbles. *Phys. Rev. Fluids* **5** (3), 033605.
- BROCCHINI, M. & PEREGRINE, D.H. 2001 The dynamics of strong turbulence at free surfaces. Part 1. Description. *J. Fluid Mech.* **449**, 225–254.
- CANO-LOZANO, J.C., MARTINEZ-BAZAN, C., MAGNAUDET, J. & TCHOUFAG, J. 2016 Paths and wakes of deformable nearly spheroidal rising bubbles close to the transition to path instability. *Phys. Rev. Fluids* **1** (5), 053604.
- CAROLI, M., DE CASTRO, P.M.M., LORIOT, S., ROULLER, O., TEILLAUD, M. & WORMSER, C. 2009 Robust and efficient Delaunay triangulations of points on or close to a sphere. *Research Rep.* RR-7004. INRIA.
- COWEN, E.A. & VARIANO, E.A. 2008 A random-jet-stirred turbulence tank. *J. Fluid Mech.* **604**, 1–32.
- DEANE, G.B. & STOKES, M.D. 2002 Scale dependence of bubble creation mechanisms in breaking waves. *Nature* **418**, 839–844.
- DEIKE, L., GHABACHE, E., LIGER-BELAIR, G., DAS, A.K., ZALESKI, S., POPINET, S. & SEON, T. 2018 Dynamics of jets produced by bursting bubbles. *Phys. Rev. Fluids* **3** (1), 013603.
- DEIKE, L. & MELVILLE, W.K. 2018 Gas transfer by breaking waves. *Geophys. Res. Lett.* **45** (19), 10–482.
- DEIKE, L., MELVILLE, W.K. & POPINET, S. 2016 Air entrainment and bubble statistics in breaking waves. *J. Fluid Mech.* **801**, 91–129.
- EGGERS, J. & VILLERMAUX, E. 2008 Physics of liquid jets. *Rep. Prog. Phys.* **71** (3), 036601.
- ELGHOBASHI, S. 2019 Direct numerical simulation of turbulent flows laden with droplets or bubbles. *Annu. Rev. Fluid Mech.* **51** (1), 217–244.
- ERN, P., RISSO, F., FABRE, D. & MAGNAUDET, J. 2012 Wake-induced oscillatory paths of bodies freely rising or falling in fluids. *Annu. Rev. Fluid Mech.* **44**, 97–121.
- FUSTER, D. & POPINET, S. 2018 An all-mach method for the simulation of bubble dynamics problems in the presence of surface tension. *J. Comput. Phys.* **374**, 752–768.
- HARPER, J.F. 1970 On bubbles rising in line at large Reynolds numbers. *J. Fluid Mech.* **41** (4), 751–758.

- HINZE, J.O. 1955 Fundamentals of the hydrodynamic mechanism of splitting in dispersion processes. *AIChE J.* **1** (3), 289–295.
- VAN HOOFT, J.A., POPINET, S., VAN HEERWAARDEN, C.C., VAN DER LINDEN, S.J.A., DE ROODE, S.R. & VAN DE WIEL, B.J.H. 2018 Towards adaptive grids for atmospheric boundary-layer simulations. *Boundary-Layer Meteorol.* **167** (3), 421–443.
- HUSSEIN, H.J., CAPP, S.P. & GEORGE, W.K. 1994 Velocity measurements in high-Reynolds number, momentum-conserving, axisymmetric, turbulent jets. *J. Fluid Mech.* **258**, 31–75.
- KOLMOGOROV, A.N. 1941 The local structure of turbulence in incompressible viscous fluid for very large Reynolds numbers. *Dokl. Akad. Nauk SSSR* **30**, 301.
- LAI, C.-Y., EGGERS, J. & DEIKE, L. 2018 Bubble bursting: universal cavity and jet profiles. *Phys. Rev. Lett.* **121**, 144501.
- LALANNE, B., MASBERNAT, O. & RISSO, F. 2019 A model for drop and bubble breakup frequency based on turbulence spectra. *AIChE J.* **65** (1), 347–359.
- LAMB, H. 1995 *Hydrodynamics*, 6th edn. Cambridge University Press.
- LANCE, M. & BATAILLE, J. 1991 Turbulence in the liquid phase of a uniform bubbly air–water flow. *J. Fluid Mech.* **222**, 95–118.
- LOISY, A. & NASO, A. 2017 Interaction between a large buoyant bubble and turbulence. *Phys. Rev. Fluids* **2**, 014606.
- MAGNAUDET, J. & EAMES, I. 2000 The motion of high-Reynolds-number bubbles in inhomogeneous flows. *Annu. Rev. Fluid Mech.* **32** (1), 659–708.
- MARTINEZ-BAZAN, C., MONTANES, J.L. & LASHERAS, J.C. 1999 On the breakup of an air bubble injected into a fully developed turbulent flow. Part 1. Breakup frequency. *J. Fluid Mech.* **401**, 157–182.
- MARTINEZ-BAZAN, C., RODRIGUEZ-RODRIGUEZ, J., DEANE, G.B., MONTAÑES, J.L. & LASHERAS, J.C. 2010 Considerations on bubble fragmentation models. *J. Fluid Mech.* **661**, 159–177.
- MASUK, A.U.M., SALIBINDLA, A., TAN, S. & NI, R. 2019 V-onset (vertical octagonal noncorrosive stirred energetic turbulence): a vertical water tunnel with a large energy dissipation rate to study bubble/droplet deformation and breakup in strong turbulence. *Rev. Sci. Instrum.* **90** (8), 085105.
- MATHAI, V., LOHSE, D. & SUN, C. 2020 Bubble and buoyant particle–laden turbulent flows. *Annu. Rev. Condens. Ma. P.* **11**, 529–559.
- MAXWORTHY, T., GNANN, C., KÜRTEEN, M. & DURST, F. 1996 Experiments on the rise of air bubbles in clean viscous liquids. *J. Fluid Mech.* **321**, 421–441.
- MILLER, C.A. & SCRIVEN, L.E. 1968 The oscillations of a fluid droplet immersed in another fluid. *J. Fluid Mech.* **32** (3), 417–435.
- MINNAERT, M. 1933 On musical air-bubbles and the sound of running water. *Phil. Mag.* **16** (104), 235–248.
- MOORE, D.W. 1965 The velocity of rise of distorted gas bubbles in a liquid of small viscosity. *J. Fluid Mech.* **23** (4), 749–766.
- MOSTERT, W. & DEIKE, L. 2020 Inertial energy dissipation in shallow-water breaking waves. *J. Fluid Mech.* **890**, A12.
- MOSTERT, W., POPINET, S. & DEIKE, L. 2021 High-resolution direct simulation of deep water breaking waves: transition to turbulence, bubbles and droplet production. [arXiv:2103.05851](https://arxiv.org/abs/2103.05851).
- PEREGRINE, D.H. 1976 Interaction of water waves and currents. *Adv. Appl. Mech.* **16**, 9–117.
- PERRARD, S., LOZANO-DURÁN, A., RABAUD, M., BENZAQUEN, M. & MOISY, F. 2019 Turbulent windprint on a liquid surface. *J. Fluid Mech.* **873**, 1020–1054.
- PHILLIPS, O.M. 1957 On the generation of waves by turbulent wind. *J. Fluid Mech.* **2** (5), 417–445.
- POPE, S.B. 2000 *Turbulent Flows*. Cambridge University Press.
- POPINET, S. 2009 An accurate adaptive solver for surface-tension-driven interfacial flows. *J. Comput. Phys.* **228**, 5838–5866.
- POPINET, S. 2015 A quadtree-adaptive multigrid solver for the Serre–Green–Naghdi equations. *J. Comput. Phys.* **302**, 336–358.
- POPINET, S. 2018 Numerical models of surface tension. *Annu. Rev. Fluid Mech.* **50**, 49–75.
- PROSPERETTI, A. 1980 Free oscillations of drops and bubbles: the initial-value problem. *J. Fluid Mech.* **100**, 333–347.
- RAVELET, F., COLIN, C. & RISSO, F. 2011 On the dynamics and breakup of a bubble immersed in a turbulent flow. *Phys. Fluids* **23**, 103301.
- REICHL, B.G. & DEIKE, L. 2020 Contribution of sea-state dependent bubbles to air-sea carbon dioxide fluxes. *Geophys. Res. Lett.* **47**, e2020GL087267.
- RISSO, F. 2018 Agitation, mixing, and transfers induced by bubbles. *Annu. Rev. Fluid Mech.* **50**, 25–48.
- RISSO, F. & FABRE, J. 1998 Oscillations and breakup of a bubble immersed in a turbulent field. *J. Fluid Mech.* **372**, 323–355.

Bubble deformation by a turbulent background

- RIVIÈRE, A., PERRARD, S., MOSTERT, W. & DEIKE, L. 2021 Sub-hinze scale bubble production in turbulent bubble break-up. *J. Fluid Mech.* (in press).
- ROSALES, C. & MENEVEAU, C. 2005 Linear forcing in numerical simulations of isotropic turbulence: physical space implementations and convergence properties. *Phys. Fluids* **17** (9), 095106.
- RUTH, D., MOSTERT, W., PERRARD, S. & DEIKE, L. 2019 Bubble pinch-off in turbulence. *Proc. Natl Acad. Sci. USA* **116** (51), 25412–25417.
- TENNEKES, H. 1975 Eulerian and lagrangian time microscales in isotropic turbulence. *J. Fluid Mech.* **67**, 561–567.
- VEJRAŽKA, J., ZEDNÍKOVÁ, M. & STANOVSKÝ, P. 2018 Experiments on breakup of bubbles in a turbulent flow. *AIChE J.* **64** (2), 740–757.
- VERON, F. 2015 Ocean spray. *Annu. Rev. Fluid Mech.* **47**, 507–538.
- VILLERMAUX, E. & BOSSA, B. 2009 Single-drop fragmentation determines size distribution of raindrops. *Nat. Phys.* **5** (9), 697.
- VORONOI, G. 1908 Nouvelles applications des paramètres continus à la théorie des formes quadratiques. *J. Reine Angew. Math.* **133**, 97–178.
- YUAN, H. & PROSPERETTI, A. 1994 On the in-line motion of two spherical bubbles in a viscous fluid. *J. Fluid Mech.* **278**, 325–349.